# Chemical evolution of disc galaxies from cosmological simulations

Milena Valentini ●,[1,2,3]★ Stefano Borgani,[3,4,5]★ Alessandro Bressan,[2,6]★
Giuseppe Murante,[3] Luca Tornatore[3] and Pierluigi Monaco[3,4]

[1]*Scuola Normale Superiore, Piazza dei Cavalieri 7, I-56126 Pisa, Italy*
[2]*SISSA – International School for Advanced Studies, via Bonomea 265, I-34136 Trieste, Italy*
[3]*INAF – Osservatorio Astronomico di Trieste, via Tiepolo 11, I-34131 Trieste, Italy*
[4]*Astronomy Unit, Department of Physics, University of Trieste, via Tiepolo 11, I-34131 Trieste, Italy*
[5]*INFN – National Institute for Nuclear Physics, Via Valerio 2, I-34127 Trieste, Italy*
[6]*INAF – Osservatorio Astronomico di Padova, Vicolo dell'Osservatorio 5, I-35122 Padova, Italy*

## ABSTRACT

We perform a suite of cosmological hydrodynamical simulations of disc galaxies, with zoomed-in initial conditions leading to the formation of a halo of mass $M_{\mathrm{halo,\,DM}} \simeq 2 \times 10^{12}$ $\mathrm{M_\odot}$ at redshift $z = 0$. These simulations aim at investigating the chemical evolution and the distribution of metals in a disc galaxy, and at quantifying the effect of (i) the assumed IMF, (ii) the adopted stellar yields, and (iii) the impact of binary systems originating SNe Ia on the process of chemical enrichment. We consider either a Kroupa, Tout & Gilmore (1993) or a more top-heavy Kroupa (2001) IMF, two sets of stellar yields and different values for the fraction of binary systems suitable to give rise to SNe Ia. We investigate stellar ages, SN rates, stellar and gas metallicity gradients, and stellar $\alpha$-enhancement in simulations, and compare predictions with observations. We find that a Kroupa et al. (1993) IMF has to be preferred when modelling late-type galaxies in the local Universe. On the other hand, the comparison of stellar metallicity profiles and $\alpha$-enhancement trends with observations of Milky Way stars shows a better agreement when a Kroupa (2001) IMF is assumed. Comparing the predicted SN rates and stellar $\alpha$-enhancement with observations supports a value for the fraction of binary systems producing SNe Ia of 0.03, at least for late-type galaxies and for the considered IMFs. Adopted stellar yields are crucial in regulating cooling and star formation, and in determining patterns of chemical enrichment for stars, especially for those located in the galaxy bulge.

**Key words:** methods: numerical – stars: abundances – ISM: abundances – galaxies: formation – galaxies: spiral – galaxies: stellar content.

## 1 INTRODUCTION

Metals are unique tracers of galaxy evolution and of the past history of feedback. Although they do not considerably contribute to the baryonic mass budget of galaxies and of their gaseous environments, they are a fundamental component of the galactic system.

Metals record earlier stages of galaxy formation, since crucial processes that shape forming galaxies and determine their evolution leave imprints on metal distribution and relative abundance of different elements. Stellar feedback pollutes the interstellar medium (ISM) with heavy metals synthesized during stellar evolution, galactic outflows fostered by both SN (supernova) explosions,

and AGN (active galactic nucleus) activity spread metals and drive them towards the circumgalactic medium (CGM), while counterbalancing and regulating the accretion of pristine or metal-poor gas from the large-scale environment (see e.g. the reviews by Veilleux, Cecil & Bland-Hawthorn 2005; Tumlinson, Peeples & Werk 2017). Some of the enriched gas that has been driven outwards from the sites of star formation within the galaxy falls then back again, eventually cooling and forming subsequent generations of stars, richer in metals than previous ones. This feedback process involves regions of the galaxy far from the original sites where outflows originated, resulting in a spread and circulation of metals over galactic scales.

A number of elements contribute to determine the present-day abundance and distribution of metals: the inital mass function (IMF), the mass-dependent lifetime function, the stellar yields, the fraction of stars in binary systems originating SNe Ia, and the efficiency and modelling of feedback processes. All these

★ E-mail: milena.valentini@sns.it (MV); borgani@oats.inaf.it (SB); sbressan@sissa.it (AB)

components are needed to build both chemodynamical models of galactic chemical evolution (along with the star formation history of the galaxy), and models of chemical evolution that are included in semi-analytical models and cosmological simulations of galaxy formation (e.g. Matteucci & Francois 1989; Chiappini, Matteucci & Gratton 1997; Gibson et al. 2003; Matteucci 2003; Nagashima et al. 2005; Tornatore et al. 2007; Borgani et al. 2008; Wiersma et al. 2009b; Yates et al. 2013; De Lucia et al. 2014; Dolag, Mevius & Remus 2017, and references therein).

The IMF determines the mass distribution that stars had at their birth and plays a crucial role in regulating the production of metals. Its shape sets the relative number of stars that enter the chemical evolution processes and those that do not, and different assumptions produce peculiar patterns of chemical enrichment. As for our Galaxy, different studies that have investigated the present-day mass function of stars located in the bulge, in the thin and thick disc agree that the IMF of MW stars, independently of their position, is compatible with a Kroupa (2001) and Chabrier (2003) IMF (see e.g. Barbuy, Chiappini & Gerhard 2018, for a recent review and references therein).

A long-standing debate concerns the universality of the IMF: observational indications suggesting that the IMF may vary depending on galaxy properties have been recently collected (e.g. Cappellari et al. 2012). The possible dependence on the metallicity, density, pressure of the gas, i.e. on the physical properties of molecular clouds, and even on the galaxy type and environment has been investigated in different studies, with no general consensus (e.g. Chiosi et al. 1998; Kroupa et al. 2013). The dependence of the IMF on the stellar mass in elliptical galaxies has been addressed with semi-analytical models. Gargiulo et al. (2015) and Fontanot et al. (2017) found that a variable IMF that depends on the instantaneous star formation rate (SFR) is suited to reproduce the observed trend of increasing $\alpha$-enhancement with larger galaxy stellar masses. These studies support a more top-heavy IMF in more massive systems. Similar findings are obtained by De Masi, Matteucci & Vincenzo (2018) using a chemical evolution model. The impact that the variation of the IMF slopes has on SFRs, galaxy morphology, chemical properties of stars, and timing of chemical enrichment has been investigated also in simulations, where different shapes of the IMF have been considered, either assuming a global IMF (Few et al. 2014) or one depending on gas density and metallicity (Bekki 2013; Gutcke & Springel 2017; Barber, Crain & Schaye 2018). Besides variations of the IMF involving the low-mass end (Conroy & van Dokkum 2012; La Barbera et al. 2013), also the number of massive stars predicted by the IMF has long been debated. By approximating the IMF with a broken power law $\phi(m) \propto m^{-\alpha}$ (Kroupa et al. 1993; Kroupa 2001; Chabrier 2003, for a review), the number density of stars per mass interval can be cast as $\phi(m) \propto m^{-2.7}$ (Kroupa et al. 1993) or $\phi(m) \propto m^{-2.3}$ (Kroupa 2001) for stars more massive than 1 $M_{\odot}$, whether the correction for unresolved binary systems is accounted for or not (Kroupa 2002; Kroupa & Weidner 2003). The impact of binary systems has been studied by Sagar & Richtler (1991), too: they found that the power-law slope $\alpha$ increases by $\sim 0.4$ if all stars are assumed to reside in binary systems.

Stellar yields contribute to determine chemical features of gas and stars. Elements released by stars in the surrounding medium control radiative cooling, regulating star formation and subsequent chemical stellar feedback. Differences between available sets of stellar yields arise because of uncertainties on stellar nucleosynthesis, and due to the details of modelling stellar evolution and the structure of the star (Karakas & Lattanzio 2007; Karakas 2010; Romano et al. 2010; Doherty et al. 2014a).

Star formation and stellar deaths affect galaxies and their CGM triggering galactic outflows. Different stellar feedback models result in different star formation histories for simulated galaxies, and the way in which galactic outflows are modeled involves how metals are distributed (Valentini et al. 2017).

Since stars retain the metals of the ISM out of which they formed, the complex interplay among the aforementioned components reflects on signatures of stars such as the $\alpha$-element-to-iron abundance ratio, $\alpha/Fe$. $\alpha$-elements (usually assumed to be O, Ne, Mg, Si, S, Ar, Ca, Ti) are metals produced as a consequence of helium nucleus captures during the Si burning phase just before the SNe II core collapse. The $\alpha/Fe$ ratio can be used to constrain the galaxy star formation history, since the trend of $\alpha$-element abundance with metallicity is determined by the time-scales of star formation and chemical enrichment, by the shape of the IMF, and by the amount of stars formed at the peak of the galaxy star formation history (Tinsley 1979). Stellar enhancement in $\alpha$-elements, with respect to the solar ratio, originates from typical time-scales of chemical enrichment. Massive stars exploding as SNe II pollute the ISM with $\alpha$-elements over a time-scale shorter than $\sim 50$ Myr, depending on the metallicity. On the other hand, the production of iron-peak elements is delayed with respect to $\alpha$-elements, since it is mainly produced by SNe Ia originating after the thermonuclear explosion of a white dwarf within a binary system. The time-scale required for SN Ia explosions and subsequent chemical feedback spans between $\sim 50$ Myr and several Gyr. This ratio allows us to identify different chemical evolutionary patterns for stars located in different components of our Galaxy, namely in the bulge, halo, or thin or thick disc (e.g. Zoccali et al. 2006; Meléndez et al. 2008).

A puzzling question pertains to the location of metals in and around galaxies. Galaxies retain some metals in their innermost regions, as heavy metals are partly locked in stars and associated with different gaseous phases of the ISM and the CGM close to the galaxy itself (e.g. Oppenheimer et al. 2012, and references therein). However, a share of the total metal budget is not confined to the nearest CGM and can be even lost beyond the galaxy virial radius. Low-density, warm CGM and IGM typically escape detections, and therefore it is difficult to probe the presence of metals several hundreds of kpc far from the galaxy centre. By focusing on studies that address the so-called missing metals problem (e.g. Bouché, Lehnert & Péroux 2005; Ferrara, Scannapieco & Bergeron 2005; Pettini 2006) at redshift $z = 0$, Gallazzi et al. (2008) found that the budget of metals locked up in stars ranges between $\sim 25$ per cent for disc-dominated galaxies and $\sim 40$ per cent in early-type galaxies. Peeples et al. (2014) investigated a sample of star-forming galaxies with stellar mass in the range $10^9 - 10^{11.5}$ $M_{\odot}$ in the local Universe and found that galaxies retain $20 - 30$ per cent of produced metals in their ISM, dust, and stars (neglecting metals locked up in stellar remnants). This fraction increases up to 50 per cent when the CGM out to 150 kpc is accounted for, with no significant dependence on the galaxy mass. Uncertainties in the adopted nucleosynthesis yields affect predictions for missing metals, since yields determine the total budget of heavy metals that one has to look for (Peeples et al. 2014).

Studying the distribution of heavy metals only in the innermost regions of galaxies provides us with a partial view. Investigating how gas flows into, within, and out of galaxies allows us to understand where the heavy metals eventually go. Cosmological hydrodynamical simulations are crucial to achieve this task, as they consistently capture the temporal and spatial complexity of gas dynamics, and account for a variety of processes, such as the chemical enrichment resulting from star formation and stellar

feedback (see e.g. Borgani et al. 2008, for a review). Some light on the origin and fate of metals in different systems have been shed by analysing the chemical properties of the ISM, CGM, IGM (intergalactic medium), and ICM (intra-cluster medium) in simulations, and comparing them with observations (e.g. Tornatore et al. 2007; Schaye et al. 2015; Biffi et al. 2017; Oppenheimer et al. 2017; Torrey et al. 2017; Vogelsberger et al. 2018). Also, chemical features of stars in simulated galaxies have been investigated. For instance, Dolag et al. (2017) investigated the stellar metallicity as a function of the galaxy stellar mass for a sample of simulated galaxies: they found a stellar mass–metallicity relation shallower than suggested by observations, simulated galaxies with stellar mass above $\sim 5 \times 10^{10}$ M$_\odot$ being, on average, not as rich in iron as observed ones. Interestingly, Grand et al. (2016) studied how the azimuthal motion of spiral arms in simulated galaxies affects the stellar metallicity distribution, promoting metal-poor stars to move inward. Furthermore, Grand et al. (2018b) investigated the metal content and $\alpha$-enhancement of stars located within galaxy discs, as a function of the distance from the galaxy centre and the height on the galactic plane, connecting chemical signatures to possible evolutionary scenarios.

The goal of this paper was to investigate the metal content of gas and stars in a suite of cosmological simulations of disc galaxies, taking advantage of our detailed model of chemical evolution. We explore the variation of the essential elements contributing to define the model of chemical evolution, with particular emphasis on the role played by the high-mass end shape of the IMF, and quantify their impact in determining metal abundance trends and evolutionary patterns. Guided by observations, we present here a detailed investigation focusing on the results at redshift $z = 0$. Comparing results with observations allows us to make predictions on some of the components of the chemical evolution model in disc galaxies, such as the IMF and the fraction of stars in binary systems that are progenitors of SNe Ia. The key questions that we want to address in our work are the following: can metallicity profiles help in supporting or discarding an IMF? Can the distribution of metals around simulated galaxies shed some light on the fate of metals? What is the impact of the different components of a chemical model on the resulting abundance pattern of gas and stars?

The outline of this paper is as follows. We introduce the simulations in Section 2. In Section 3, we quantify the impact of two different IMFs on the predicted number of massive stars. In Section 4, we present and discuss our results. Section 4.1 provides an overview of the main features of our simulated galaxies, and in Section 4.2 we analyse stellar ages and SN rates. We then investigate the matal content of gas and stars, focusing on metallicity profiles (Section 4.3) and stellar $\alpha$-enhancement (Section 4.4). We study the distribution of metals around galaxies in Section 4.5, and the impact of adopted stellar yields in Section 4.6. We summarize our key results and draw conclusions in Section 5.

## 2 NUMERICAL SIMULATIONS

### 2.1 Initial conditions and simulation set-up

In this work we perform a suite of cosmological hydrodynamical simulations with zoomed-in initial conditions (ICs) describing an isolated dark-matter (DM) halo of mass $M_{\text{halo, DM}} \simeq 2 \times 10^{12}$ M$_\odot$ at redshift $z = 0$. These ICs are identified as *AqC* and have been first introduced by Springel et al. (2008) for the DM component. The zoomed-in region that we simulate has been selected within

a cosmological volume of $100 \,(h^{-1}\, \text{Mpc})^3$ of the DM-only parent simulation. We adopt a $\Lambda$CDM cosmology, with $\Omega_{\text{m}} = 0.25$, $\Omega_\Lambda = 0.75$, $\Omega_{\text{baryon}} = 0.04$, $\sigma_8 = 0.9$, $n_{\text{s}} = 1$, and $H_0 = 100 \, h$ km s$^{-1}$ Mpc$^{-1} = 73$ km s$^{-1}$ Mpc$^{-1}$. The Lagrangian region of the forming halo is sampled with the higher resolution DM particles. Each of these particles has been split into a DM plus a gas particle according to the adopted baryon fraction so as to have ICs for both DM and baryons (as in Scannapieco et al. 2012). Baryons and high-resolution DM particles define a Lagrangian volume that, by $z = 0$, entirely contains a sphere of $\sim 3$ Mpc radius centred on the main galaxy formed (this piece of information will be exploited in Section 4.5).

The simulated halo does not experience major mergers at low redshift and does not have close massive satellite galaxies, thus it is expected to host a disc galaxy at redshift $z = 0$. While some of the simulated galaxies are similar to our Galaxy from the morphological point of view, our results should not be deemed as a model of the MW, as no specific attempts to reproduce the accretion history of its dynamical environment have been made.

The simulations have been carried out with the TreePM + SPH (smoothed particle hydrodynamics) GADGET3 code, a non-public evolution of the GADGET2 code (Springel 2005). In this version of the code we adopt the improved formulation of SPH introduced in Beck et al. (2016). This implementation accurately samples the fluid, properly describes and follows hydrodynamical instabilities, and removes artificial viscosity away from shock regions, as it includes a higher order kernel function, an artificial conduction term and a correction for the artificial viscosity. This new SPH formulation has been introduced in cosmological simulations adopting our sub-resolution model MUPPI (MUlti Phase Particle Integrator; Murante et al. 2010, 2015) according to Valentini et al. (2017). MUPPI describes a multiphase ISM featuring star formation and stellar feedback, metal-dependent cooling and chemical enrichment, and also accounts for the presence of an ionizing cosmic background (see Section 2.2).

In our simulations the Plummer-equivalent softening length for the computation of the gravitational force is $\varepsilon_{\text{Pl}} = 325 \, h^{-1}$ pc, constant in comoving units down to $z = 6$, and constant in physical units at lower redshift. Mass resolutions for DM and gas particles are as follows: DM particles have a mass of $1.6 \times 10^6 \, h^{-1}$ M$_\odot$, while the initial mass of gas particles is $3.0 \times 10^5 \, h^{-1}$ M$_\odot$. The mass of gas particles is not constant throughout the simulation, since the initial mass can increase due to gas return by neighbour star particles and decrease because of star formation.

The key features of our sub-resolution model are outlined in Section 2.2, while the simulations carried out for the present investigation are introduced in Section 2.3.

### 2.2 Stellar feedback and chemical enrichment

Our simulations resort to the sub-resolution model MUPPI to describe processes that occur on scales not explicitly resolved. A thorough description of the model can be found in Murante et al. (2010, 2015) and Valentini et al. (2017, 2018): in this section we recall its most important features, while we refer the reader to the aforementioned papers for any further details. Our sub-resolution model describes a multiphase ISM. Its fundamental element is the multiphase particle that consists of a hot and cold gas phases in pressure equilibrium, plus a possi-

ble stellar component. A gas particle enters a multiphase stage whenever its density increases above a density threshold ($n_{thres} = 0.01$ cm$^{-3}$) and its temperature drops below a temperature threshold ($T_{thresh} = 10^5$ K).

A set of ordinary differential equations describes mass and energy flows among different components: hot gas condenses into a cold phase (whose temperature is fixed to $T_c = 300$ K) due to radiative cooling, while some cold gas evaporates due to the destruction of molecular clouds. A fraction of the cold gas mass is in the molecular phase: it can be converted into stars according to a given efficiency that allows to compute the instantaneous SFR of the multiphase particle. Star formation is implemented according to the stochastic model of Springel & Hernquist (2003).

Sources of energy counterbalancing radiative cooling are the energy contributed by stellar feedback (see below) and the hydrodynamical term that accounts for shocks and heating or cooling due to gravitational compression or expansion of gas. A gas particle exits the multiphase stage whenever its density decreases below a threshold or after a maximum allowed time given by the dynamical time of the cold gas phase. A gas particle eligible to quit a multiphase stage has a probability of being kicked and to become a wind particle for a given time interval, during which it is decoupled from the surrounding medium. This probability is a parameter of our subresolution model (in all the simulations presented in this paper, we assume a value of 0.03). This model relies on the assumption that galactic winds are powered by SN II explosions, once the molecular cloud out of which stars formed has been destroyed. While being decoupled, wind particles can receive kinetick feedback energy, as described below.

We account for stellar feedback in both thermal (Murante et al. 2010) and kinetic (Valentini et al. 2017) forms. As for thermal feedback, if a particle is multiphase, its hot gas component is heated by the energy injected by SN explosions within the stellar component of the particle itself, a fraction $f_{fb, local}$ of $E_{SN} = 10^{51}$ erg being deposited in its hot gas component. Also, SNe in neighbouring star-forming particles provide energy to both single-phase and multiphase gas particles, this energy being supplied to the hot gas phase if the particle is multiphase.

As for the kinetic stellar feedback, multiphase particles provide the ISM with kinetic feedback energy isotropically. Each star-forming particle supplies the energy $f_{fb, kin} E_{SN}$ to all wind particles within the smoothing length, with kernel-weighted contributions. $f_{fb, kin}$ describes the kinetic stellar feedback efficiency. Wind particles receiving energy use it to increase their velocity along their least resistance path, since they are kicked against their own density gradient. Kinetic stellar feedback is responsible for triggering galactic outflows. This model for kinetic stellar feedback and galactic outflows promotes the formation of disc galaxies with morphological, kinematic, and chemical properties in keeping with observations (Valentini et al. 2017, 2018).

Star formation and evolution also produce a chemical feedback. In our model, chemical evolution and enrichment processes are accounted for according to the model of Tornatore et al. (2007), where a detailed description can be found. Here we only highlight the most relevant features of the model. Star particles are considered to be simple stellar populations (SSPs). We evaluate the number of aging and eventually exploding stars, along with the amount of metals returned to the ISM, assuming an IMF and adopting stellar lifetimes and stellar yields (see Section 2.3 for details). Metals produced and released by star particles are distributed to neighbouring gas particles within the star particles' smoothing

**Table 1.** Relevant features of the simulation suite. Column 1: simulation label. Column 2: adopted IMF. Column 3: set of yields. Set A: Thielemann et al. (2003); Karakas (2010); Woosley & Weaver (1995); Romano et al. (2010). Set B: Thielemann et al. (2003); Karakas (2010); Doherty et al. (2014a,b); Nomoto, Kobayashi & Tominaga (2013). See the text for details. Column 4: fraction of binary systems originating SN Ia. Column 5: kinetic SN feedback energy efficiency.

| Name | IMF | Set of yields | $f_{fb, Ia}$ | $f_{fb, kin}$ |
|------|-----|---------------|--------------|---------------|
| K2s–yA–IaA–kA | Kroupa (2001) K2s, equation (2) | A | 0.1 | 0.12 |
| K2s–yA–IaB–kA | Kroupa (2001) K2s, equation (2) | A | 0.03 | 0.12 |
| K3s–yA–IaA–kB | Kroupa et al. (1993) K3s, equation (3) | A | 0.1 | 0.26 |
| K3s–yA–IaB–kB | Kroupa et al. (1993) K3s, equation (3) | A | 0.03 | 0.26 |
| K2s–yB–IaB–kA | Kroupa (2001) K2s, equation (2) | B | 0.03 | 0.12 |
| K3s–yB–IaB–kB | Kroupa et al. (1993) K3s, equation (3) | B | 0.03 | 0.26 |

sphere,[1] so that subsequently generated star particles are richer in heavy elements. We follow in details the chemical evolution of the following elements, produced by AGB (asymptotic giant branch) stars, SNe Ia and SNe II: H, He, C, N, O, Ne, Na, Mg, Al, Si, S, Ar, Ca, Fe, and Ni. Each element independently contributes to the cooling rate, which is implemented according to Wiersma, Schaye & Smith (2009a). When computing cooling rates, the effect of a spatially uniform, time-dependent ionizing cosmic background (Haardt & Madau 2001) is accounted for.

Besides those described in Section 2.3 and listed in Table 1, all the relevant parameters of our sub-resolution model that we adopt for this set of simulations can be found in Valentini et al. (2018) (Table 1), considering the simulation labeled AqC5–fid. It is worth noting that our sub-resolution model does not have parameters that have been calibrated to reproduce observations of metal abundances in the ISM and CGM (for instance, at variance with Vogelsberger et al. 2013; Pillepich et al. 2018), we do not adopt a wind metal loading factor to regulate the metallicity of the wind relative to that of the ISM from where the wind originated).

### 2.3 The set of simulations

In this work we consider results of six simulations that we carried out. We list them in Table 1. These simulations have been conceived so as to investigate and quantify the effect of the adopted IMF and stellar yields, along with the impact of binary systems originating SN Ia on the chemical enrichment process.

We define the IMF $\phi(m)$:

$$\phi(m) = \beta m^{-\alpha} \tag{1}$$

as the number of stars per unit mass interval, in the mass range $[M_{inf}, M_{sup}]$. We consider two IMFs: the Kroupa (2001) IMF and

---

[1]By analogy with gas particles, the mass within the sphere whose radius is the star particle smoothing length is required to be constant and equal to that enclosed within the gas particles' smoothing sphere.
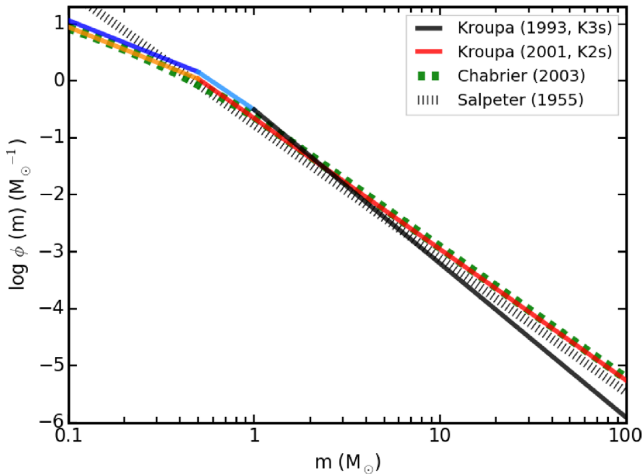
**Figure 1.** Stellar number distribution per mass interval as a function of the mass for the two IMFs that we are considering for the current analysis: K2s is the Kroupa (2001) IMF described by equation (2), while K3s is the Kroupa et al. (1993) IMF represented by equation (3). For reference, we also show the Chabrier (2003) IMF and the Salpeter (1955) IMF.

the Kroupa et al. (1993) IMF. We choose these two IMFs because one focus of our study is to investigate the impact of the number of massive stars on the metal production. We note that the Kroupa (2001) IMF is almost indistinguishable by the widely adopted Chabrier (2003) IMF (see Fig. 1): therefore, by considering the Kroupa (2001) and the Kroupa et al. (1993) IMFs we examine the possible variation of the high-mass end shape of the IMF. The Kroupa (2001) IMF (K2s, hereafter) is characterized by the following values for the slope $\alpha$ of the power law in different mass intervals:

$$\alpha = 1.3 \quad \text{for} \quad 0.08 \, \text{M}_\odot \le m \le 0.5 \, \text{M}_\odot,$$

$$\alpha = 2.3 \quad \text{for} \quad 0.5 \, \text{M}_\odot < m \le 100 \, \text{M}_\odot. \tag{2}$$

We adopt $M_{\text{inf}} = 0.08 \, \text{M}_\odot$ and $M_{\text{sup}} = 100 \, \text{M}_\odot$ for K2s. The IMF slope $\alpha = 2.3$ for massive stars is not corrected for unresolved stellar binaries (see below). For each mass interval, a normalization constant $\beta$ is computed by imposing that $\int m \, \phi(m) \, dm = 1$ over the global mass range and continuity at the edges of subsequent mass intervals.

The second IMF that we adopt is the Kroupa et al. (1993) IMF (K3s, hereafter). This IMF is characterized by three slopes, as $\alpha$ in equation (1) has the following values according to the mass interval:

$$\alpha = 1.3 \quad \text{for} \quad 0.1 \, \text{M}_\odot \le m \le 0.5 \, \text{M}_\odot,$$

$$\alpha = 2.2 \quad \text{for} \quad 0.5 \, \text{M}_\odot < m \le 1.0 \, \text{M}_\odot,$$

$$\alpha = 2.7 \quad \text{for} \quad 1.0 \, \text{M}_\odot < m \le 100 \, \text{M}_\odot. \tag{3}$$

It is defined in the mass range [0.1, 100] $\text{M}_\odot$ (as suggested by Matteucci & Gibson 1995; Grisoni et al. 2017). In this case, the slope $\alpha = 2.7$ for massive stars includes the correction for unresolved stellar binary systems (Kroupa 2002). This correction accounts for the large fraction (more than $\sim$50 per cent) of stars that are located in binary systems. Surveys in our Galaxy that observe and count stars often lack the resolution to resolve pairs

of close stars. The resulting statistics is therefore biased towards larger mass stars, because a fraction of them actually come from the superposition of lower mass stars. Correcting for this effect leads to a steepening of the slope in the high-mass range (Sagar & Richtler 1991; Kroupa 2002; Kroupa & Weidner 2003, see also Section 1).

We account for different evolutionary time-scales of stars with different masses by adopting the mass-dependent lifetimes by Padovani & Matteucci (1993). Stars with an initial mass larger than $M_{\text{up}}$ and lower than $M_{\text{sup, SNII}} = 40 \, \text{M}_\odot$ are assumed to end their life exploding as core-collapse SNe. We consider $M_{\text{up}} = 8 \, \text{M}_\odot$, except when the set B of yields is used (see below). In this latter case $M_{\text{up}} = 9 \, \text{M}_\odot$ (see Section 3, too). Stars that are more massive than 40 $\text{M}_\odot$ are assumed to implode in BHs directly, and thus do not contribute to further chemical enrichment or stellar feedback energy.

A fraction of stars relative to the whole mass range is assumed to be located in binary systems that are progenitors of SNe Ia. According to the model by Greggio & Renzini (1983) and adopting the same formalism as in Tornatore et al. (2007), the rate of SN Ia explosions can be cast as

$$R_{\text{SNIa}}(t) = -\frac{\text{d}m(t)}{\text{d}t}\bigg|_{m_2 \equiv \tau^{-1}(t)} \cdot 24 \, m_2^2 \, A \int_{M_{\text{B,m}}}^{M_{\text{B,M}}} \phi(m_{\text{B}}) \, \frac{1}{m_{\text{B}}^3} \, \text{d}m_{\text{B}}. \tag{4}$$

In equation (4), $\tau^{-1}(t)$ is the inverse of the lifetime function $\tau(m)$, which describes the age at which a star of mass $m$ dies, $-\text{d}m(t)/\text{d}t$ accounts for the mass of stars dying at time $t$, and $m_2$ is the mass of the secondary star in the binary system (within the single-degenerate scenario, as in the formulation of Greggio & Renzini 1983). Also, $A$ is the fraction of stars in binary systems suitable to host SNe Ia (see below), and $\phi(m)$ is the IMF. The integral in equation (4) is computed over the total mass of the binary system $m_{\text{B}}$ producing an SN Ia, which varies from $M_{\text{B, m}} = 3 \, \text{M}_\odot$ to $M_{\text{B, M}} = 16 \, \text{M}_\odot$ (or from 3 to 18 $\text{M}_\odot$ when using the set B of yields).[2] The first SNe Ia explode therefore in binary systems whose components have both an initial mass of 8 $\text{M}_\odot$ (or 9 $\text{M}_\odot$), according to the single-degenerate scenario. This determines the time-scale required for SN Ia explosions and consequent chemical enrichment that ranges between $\sim$50 Myr and several Gyr ($\sim$50 per cent of the total SNe Ia in an SSP explode after $\sim$1 Gyr). Since SNe Ia are the main source for the production of iron-peak elements, their rate impacts directly on abundance trends and evolutionary patterns. In order to constrain the SN Ia rate, we explore the variation of the probability of the realization of a binary system hosting an SN Ia (while we do not consider to account for possible variations of stellar lifetimes or the distribution function of delay times). We consider two values for the fraction of binary systems giving rise to SN Ia: either $f_{\text{bin, Ia}} = 0.1$ (case A; Greggio & Renzini 1983; Matteucci & Greggio 1986; Tornatore et al. 2007) or $f_{\text{bin, Ia}} = 0.03$ (case B; as suggested by Grisoni et al. 2017). This parameter is commonly referred to as $A$ (see equation 4), but we prefer to call it $f_{\text{bin, Ia}}$ from now on (in order not to be confused with letters A and B in the simulation labels; see Table 1). In general, it depends on the adopted IMF, on the systems and environments

---

[2]We note that slightly different metrics can be used when computing the number of SNe Ia. For instance, Maoz (2008) provides several estimates to compute the SN Ia explosion fractions. Also, an interesting comparison between different SN Ia progenitor models is presented in Few et al. (2014).

investigated (Matteucci & Gibson 1995), and other values have been adopted as well (e.g. Spitoni & Matteucci 2011). We note that assuming the same fraction of binary systems when two IMFs are considered does not lead to the same number of SN Ia explosions.

We follow the production of different heavy metals by stars that evolve and eventually explode adopting stellar yields. We consider two sets of stellar yields in order to quantify the impact that they have on final results. In the first set of yields, which we refer to as set A, we assume yields tabulated by Thielemann et al. (2003) for SNe Ia, while we adopt the mass- and metallicity-dependent yields by Karakas (2010) for AGB stars. Also, we use the mass- and metallicity-dependent yields by Woosley & Weaver (1995) for SNe II, combined with the prescriptions provided by Romano et al. (2010) for the Fe, Si, and S production. As for the second set of yields, labeled as set B, we adopt the stellar yields provided by Thielemann et al. (2003) for SNe Ia and the mass- and metallicity-dependent yields by Nomoto et al. (2013) for SNe II. We use the mass- and metallicity-dependent yields by Karakas (2010) and Doherty et al. (2014a,b) for low and intermediate mass stars that undergo the AGB and super-AGB phase (7−9 M$_\odot$). These sets of yields have been tested by state-of-the-art chemical models and well reproduce observations of different ion abundances in the MW (Romano et al. 2010, 2017, and private communications). The difference between these two sets of stellar yields is quantified in Section 4.6.

The key features of our simulations are listed in Table 1. Besides the name and the resolution of the ICs, i.e. *AqC5*, the simulation label encodes the adopted IMF, the considered set of stellar yields, and two parameters, namely the value of binary systems giving rise to SNe Ia and the kinetic stellar feedback efficiency, respectively.

## 3 IMPACT OF IMF ON THE NUMBER OF MASSIVE STARS

Stellar feedback is one of the natural outcomes of star formation, but it also contributes to regulate it. Therefore, should the number of stars that mainly contribute to stellar feedback vary as a consequence of a different IMF, the amount of feedback energy is directly affected, with a dramatic impact on the star formation history of the galaxy. The number of stars that end up their life as SNe II deserves particular attention, as they mainly contribute to determine the available kinetic feedback energy and to trigger galactic outflows, expelling gas outwards.

Fig. 1 shows the number density distribution per mass interval as a function of the mass for the two IMFs that we are considering for the current analysis (see equations 2 and 3 for K2s and K3s IMFs, respectively).

The number of massive (m > M$_{up}$) stars exploding as SNe II in an SSP assuming an IMF $\phi(m) = A_\phi \, m^{-\alpha}$ is

$$N_{*\mathrm{massive}} = A_\phi \int_{M_{\mathrm{up}}}^{M_{\mathrm{sup, SNII}}} m^{-\alpha} \, \mathrm{d}m \quad , \tag{5}$$

$A_\phi$ being the normalization constant and $\alpha$ the slope of the adopted IMF in the considered mass range, respectively. In equation (5), $M_{\mathrm{up}}$ is the initial mass threshold for massive stars that explode as SNe II and $M_{\mathrm{sup, SNII}}$ is the upper bound of the initial mass range in which stars are assumed to end their life as core-collapse SNe. We assume $M_{\mathrm{sup, SNII}} = 40 \, \mathrm{M}_\odot$.

For K2s $\phi(m) \simeq 0.22 \, m^{-2.3}$ for m > M$_{up}$, while for K3s $\phi(m) \simeq 0.31 \, m^{-2.7}$. Integrating equation (5) over the mass range and assuming M$_{up}$ = 8 M$_\odot$ yields to the following numbers of massive stars: $N_{*\mathrm{massive, K2s}} \simeq 0.994 \times 10^{-2}$ for K2s, and $N_{*\mathrm{massive, K3s}} \simeq 0.497 \times 10^{-2}$ when K3s is adopted. Thus, K2s predicts roughly twice as many massive stars as K3s. This reflects directly in the amount of stellar feedback energy that the ISM is provided with. Therefore, in order to have a comparable amount of feedback energy from SN explosions, the kinetic stellar feedback efficiency $f_{\mathrm{fb, kin}}$ has to be doubled in simulations adopting the K3s IMF (i.e. $f_{\mathrm{fb, kin}}$ = 0.26).

We note that marginal variations of the mass interval over which the integral in equation (5) is computed do not influence significantly the ratio of massive stars when the different IMFs are considered. For instance, there is not general consensus on the exact value of $M_{\mathrm{up}}$ in the range 7−9 M$_\odot$, mainly because of the modelling of convection within the star. Assuming $M_{\mathrm{up}} = 9 \, \mathrm{M}_\odot$ (instead of $M_{\mathrm{up}} = 8 \, \mathrm{M}_\odot$) as the lower limit of integration in equation (5) does not impact significantly on the relative number of $N_{*\mathrm{massive}}$ nor on final results. We actually assume $M_{\mathrm{up}} = 9 \, \mathrm{M}_\odot$ in simulations adopting the set B of stellar yields, as Doherty et al. (2014a,b) consider that stars with initial mass ranging between 7 and 9 M$_\odot$ undergo the super-AGB phase.

Accounting properly for the number of SNe II and recalibrating the feedback efficiency accordingly allows us to have a comparable star formation history for simulations K2s–yA–IaA–kA and K3s–yA–IaA–kB (see Fig. 3 and Section 4.1). We emphasize that this is the reason why we decide to contrast results from simulations adopting the K2s IMF and $f_{\mathrm{fb, kin}}$ = 0.12 (kA in simulation names), and the ones with the K3s IMF and $f_{\mathrm{fb, kin}}$ = 0.26 (kB in simulation labels) when analysing the effect of the varying IMF. The total stellar feedback energy is still reduced when the K3s IMF is assumed. Nonetheless, we are interested primarily in the kinetic stellar feedback, as it is responsible for the triggering of galactic outflows, whose role is key in controlling gas accretion, gas ejection, and star formation (see also Valentini et al. 2017).

At variance with our aforementioned recalibration, Gutcke & Springel (2017) did not tune the stellar feedback efficiency accounting for the different number of stars produced by the adopted metallicity-dependent IMF, with a consequent overproduction of stellar mass resulting from a modified star formation history.

## 4 RESULTS

In this section we present our results. In Section 4.1 we show the main properties of the simulated galaxies. In Section 4.2 we analyse stellar ages and SN rates, while in Section 4.3 we show radial abundance profiles for gas and stars in our set of galaxies. In Sections 4.4 and 4.5 we investigate the $\alpha$-enhancement of stars and where metals are located within and around our galaxies. In Section 4.6 we investigate how stellar yields impact on final results.

Throughout this paper, when we mention metallicity we refer to the abundance by the number of a given element or ratio between two elements. When comparing element abundance to that of Sun, we adopt values for the present-day Sun's abundance in the element $X$ (i.e. $\log_{10}\varepsilon_X = 12 + \log_{10}(N_X/N_H)$, where $N_X$ and $N_H$ are number densities of the element $X$ and of hydrogen, respectively) according to Caffau et al. (2011, as for iron) and to Asplund et al. (2009, for all the other elements).

## 4.1 Main properties of the simulated galaxies

We introduce the main physical properties of the galaxies resulting from our cosmological simulations. Fig. 2 shows projected stellar (first and second columns) and gas (third and fourth columns) density maps for each galaxy. Both edge-on (first and third columns) and face-on (second and fourth columns) views are presented. Galaxies have been rotated so that the *z*-axis of their reference system is aligned with the angular momentum of star particles and cold and multiphase gas particles located within 8 kpc from the minimum of the gravitational potential. The centre of the galaxy, where the origin of the reference system is set, is assumed to be the centre of mass of the aforementioned particles. Here and in the following text, we consider for our analysis star and gas particles that are located within the galactic radius,[3] unless otherwise stated. The galactic radius of these galaxies is $R_{gal} \sim 24$ kpc.

Density maps in Fig. 2 show that all the galaxies but K2s–yA–IaB–kA and K2s–yB–IaB–kA have a limited bulge and a dominant disc component, although the morphology and the extent of the disc vary from galaxy to galaxy. In particular, some galaxies exhibit an irregular distribution of gas around and above the galactic plane, thus suggesting ongoing gas accretion (see also Fig. 4). A clear spiral pattern is evident in the majority of the discs.

In Fig. 3 we show the evolution of the SFR of the six galaxies. A high-redshift ($z \gtrsim 3$) star formation burst characterizes the star formation history of all the galaxies, in a remarkably similar way, building up the bulk of the stellar mass in the bulge of each galaxy. Star formation occurring at lower redshift, in a more continuous way, is then responsible of the (possible) formation of the disc. General trends are as follows: the lower the fraction of binary systems originating SNe Ia, the lower the SFR below $z \sim 1$. Also, the set B of stellar yields is responsible for the reduced gas cooling and consequent lower SFR. This is particularly evident when contrasting the SFR of K3s–yA–IaB–kB and K3s–yB–IaB–kB. The reason stems from the lower amount of iron that is produced when reducing the number of SNe Ia, the iron being one of the main coolants (along with oxygen, for solar abundances; Wiersma et al. 2009a). Also, the stellar yields labeled as B predict a lower synthesis of Fe for all the considered metallicities and a lower production of O for solar metallicity (see Sections 4.4 and 4.6). Effects on the star formation are evident, as a consequence of the element-by-element metal cooling in our simulations.

A complex interplay between different processes determines and regulates the star formation histories of the galaxies in Fig. 3: the reservoir of gas available for star formation, the cooling process, and stellar feedback. Fig. 4 shows the mass accretion history of gas within the galactic radius $R_{gal}$ for the main progenitor of each galaxy: it quantifies the mass of gas within $R_{gal}$, and how inflows and outflows impact on the amount of gas within $R_{gal}$ across cosmic time. It can be related to the evolution of the SFR. However, there is not a direct correspondance between the amount of accreted gas and the SFR. The reason is that gas accreted becomes available for star formation as soon as it approaches the innermost regions of the forming galaxy and cools. Besides on density, gas cooling depends on metallicity that primarily shapes the cooling function.

---

[3]We define here the galactic radius as one-tenth of the virial radius, i.e. $R_{gal} = 0.1R_{vir}$. We choose the radius $R_{gal}$ so as to identify and select the region of the computational domain that is dominated by the central galaxy. Moreover, we consider virial quantities as those computed in a sphere that is centred on the minimum of the gravitational potential of the halo and that encloses an overdensity of 200 times the *critical* density at present time.

Also, massive stars trigger galactic outflows as they explode as SNe II: outflows can hamper gas that is accreted within the virial radius from flowing inwards and feed star formation. A more top-heavy IMF (i.e. K2s) would further affect this scenario if the feedback efficiency were not calibrated (see Section 3). We note that minor variations between low-redshift star formation histories and gas mass accretion histories of galaxies with different IMFs are present, despite the feedback efficiency calibration: this is a further evidence of how different elements enter the process of galaxy formation in a non-linear fashion. Also, the formation of the stellar disc is highly sensitive to the timing of gas accretion (see also Valentini et al. 2017).

Fig. 5 presents a kinematic decomposition of simulated galaxies. We examine the circularity of stellar orbits in order to distinguish between the rotationally and dispersion-supported components of each galaxy, thus quantifying the prominence of the disc with respect to the bulge. The circularity of stellar orbits is defined as the ratio of specific angular momenta $J_z/J_{circ}$, where $J_z$ is the specific angular momentum in the direction perpendicular to the disc, and $J_{circ}$ is the angular momentum of a reference circular orbit at the considered distance from the galaxy centre (Scannapieco et al. 2009). Stars located in the disc contribute to the peak where $J_z/J_{circ} = 1$, while stars in the bulge are characterized by $J_z/J_{circ} \sim 0$. Galaxies K3s–yA–IaA–kB and K2s–yA–IaA–kA exhibit the most pronounced disc, as a consequence of the higher low-redshift SFR (see Fig. 3). An extended disc where the bulk of the stellar mass is located characterizes galaxies K3s–yA–IaB–kB and K3s–yB–IaB–kB, while K2s–yB–IaB–kA has a smaller stellar disc component. Finally, K2s–yA–IaB–kA is an irregular galaxy with a dominant spheroidal component (as shown in Fig. 2). Table 2 summarizes the morphological features of different galaxy models and whether galaxy properties meet or not observational constraints that we consider during our analysis throughout Section 4. The prominence of the stellar disc can be easily explained by analysing the SFR below $z \sim 1$ in Fig. 3. A higher low-redshift SFR translates directly in a more extended stellar disc component. Stellar masses of galaxies and bulge-over-total (B/T) mass ratios are as follows: $3.64 \times 10^{10}$ M$_\odot$ and 0.33 (K2s–yA–IaA–kA), $2.02 \times 10^{10}$ M$_\odot$ and 0.97 (K2s–yA–IaB–kA), $3.85 \times 10^{10}$ M$_\odot$ and 0.28 (K3s–yA–IaA–kB), $2.68 \times 10^{10}$ M$_\odot$ and 0.41 (K3s–yA–IaB–kB), $2.06 \times 10^{10}$ M$_\odot$ and 0.64 (K2s–yB–IaB–kA), $2.24 \times 10^{10}$ M$_\odot$ and 0.45 (K3s–yB–IaB–kB).

We note that our estimate for the B/T ratio could also include satellites, stellar streams, and contribution from bars within $R_{gal}$. Therefore, the B/T values that we quote should not be directly compared with observational photometric estimates, as the photometric determination for the value of B/T has been shown to be lower than the corresponding kinematic estimate (Scannapieco et al. 2010).

## 4.2 Stellar ages and SN rates

We continue our analysis by investigating stellar ages and formation epochs for different components of our galaxies. Fig. 6 shows radial profiles of the mass-weighted age of stars within the galactic radius for the six simulations. The corresponding redshift at which stars form is displayed, too. Stars in the innermost regions of galaxies have, on average, an age ranging between 9.5 and 11 Gyr, depending on the simulation. The mass-weighted mean age of stars progressively decreases as the distance from the galaxy centre increases and a minimum is reached in correspondence with the extent of the stellar disc of each galaxy. Moving then outwards, the mean stellar age of the stars progressively increases. When
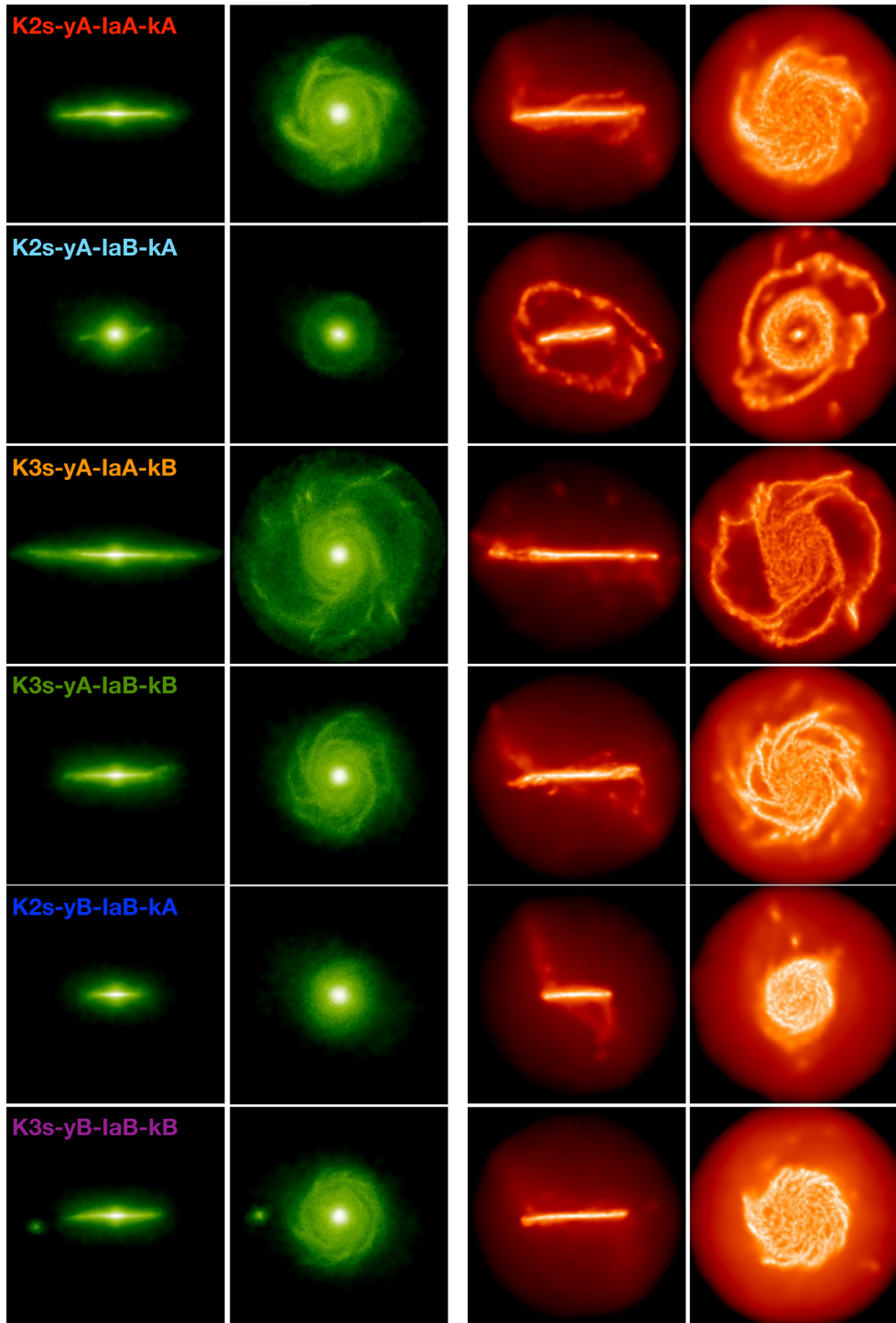
**Figure 2.** Projected stellar (first and second columns) and gas (third and fourth columns) density maps for the set of simulated galaxies listed in Table 1, at redshift $z = 0$. Each row shows a galaxy, whose name is indicated in the first column panel. First and third columns show edge-on galaxies, and second and fourth columns depict face-on maps. The size of each box is 48 kpc a side.

computing the age of stars located at an increasing distance from the galaxy centre, we consider stars within spherical shells with a given radial thickness. Therefore, albeit the identification of the innermost and outermost old stars with bulge and halo stars, respectively, is straightforward, stars that make the radial profile decline cannot be associated directly to the disc component.

For this reason, in order to further investigate stellar ages for stars in the disc, we focus on simulation K3s–yA–IaB–kB and consider a region limited as follows: $3 < r < 13$ kpc and $|z| < 5$ kpc, $r$ and $z$ being the radial distance from the galaxy centre and the galactic latitude, respectively. We show the mass-weighted age of stars in the aforementioned volume that can be deemed as the disc (green dashed
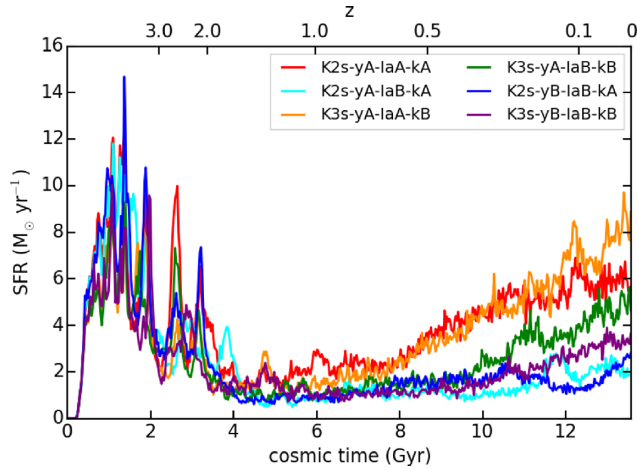
**Figure 3.** Star formation histories for the six simulated galaxies listed in Table 1. Red curve shows K2s–yA–IaA–kA, and cyan and orange lines depict K2s–yA–IaB–kA and K3s–yA–IaA–kB, respectively. The green curve refers to K3s–yA–IaB–kB, while blue and purple lines show K2s–yB–IaB–kA and K3s–yB–IaB–kB, respectively (as shown in the legend).



**Figure 5.** Stellar mass as a function of the circularity of stellar orbits at $z = 0$ for the set of galaxies. The height of the peaks at $J_z/J_{circ} = 0$ and at $J_z/J_{circ} = 1$ shows the relative contribution to the total stellar mass of the bulge and the disc, respectively. Bulge-over-total mass ratios are as follows: 0.33 (red), 0.97 (cyan), 0.28 (orange), 0.41 (green), 0.64 (blue), and 0.45 (purple).



**Figure 4.** Mass accretion history (MAH) of gas within the galactic radius $R_{gal}$ of galaxies. We show the redshift evolution of the mass of gas that is within $R_{gal}$ of the main progenitor of our simulated galaxies. Colours as in Fig. 3.

the galaxy models where studying stars in the disc. Note that the stellar age profile of stars in the disc of K3s–yA–IaB–kB is flatter than the profile characterizing all the stars in that considered range of distance from the galaxy centre, younger stars at higher latitudes on the galactic plane being not included.

Inspecting the stellar age of K3s–yA–IaB–kB further, we show the face-on and edge-on distribution of all the star particles within the galactic radius $R_{gal}$ at redshift $z = 0$ in Fig. 7. The colour encodes the mean age of the star particles in each spatial bin: we can appreciate how the stellar age changes as a function of the distance from the galaxy centre across the galactic plane (left-hand panel of Fig. 7) and as a function of the galactic latitude (right-hand panel). The youngest stars trace the spiral pattern of the galaxy, and pinpoint spiral arms as sites of recent star formation. The thickness of the stellar disc progressively increases moving outwards. The halo and the bulge are made up of the oldest stars in galaxy.

When analysing stellar ages at $z = 0$ in Figs 6 and 7, we analyse mean quantities, thus it is not trivial to deduce straightforwardly the formation scenario. If we consider the distribution in Fig. 7 at higher-redshift simulation outputs (i.e. by evolving it backward in time), we find that high-$z$ star formation occurs first in the innermost regions of the forming galaxy and soon after it is widespread in the galaxy, the oldest (∼12 Gyr) stars spreading across the halo as well as in inner regions (see Clemens et al. 2009, for a similar scenario in elliptical galaxies). As time passes, star formation involves internal regions alone, as they are replenished with gas that is accreted from the large-scale environment, and takes place especially in the forming bulge and at relatively larger distances from the centre with few episodes of star formation. Then, at later epochs ($z \lesssim 1.5$), star formation in the disc occurs and the disc formation proceeds inside-out.

The presence of an old (∼12 Gyr) stellar component throughout the galaxy can be seen in Fig. 8, where the distribution of stellar mass per bin of lookback time is shown. The galaxy stellar content has been sliced into four different regions (within the galactic radius, $r < R_{gal}$), as reported in each panel. The regions can be considered as a representative of the following components of the galaxy: bulge (top left), inner disc (top right), outer disc (bottom left), and halo

line) in Fig. 6, too. Stars are characterized by a negative age radial gradient, and this supports the inside-out growth for the stellar disc. This scenario, where stellar discs progressively increase their size as they evolve and grow more massive, is corroborated by a variety of observations (e.g Barden et al. 2005; Muñoz-Mateos et al. 2011; Patel et al. 2013; González Delgado et al. 2014), and by models of chemical evolution (e.g. Chiappini, Matteucci & Romano 2001), by semi-analytical models (e.g. Dutton et al. 2011), and simulations (e.g. Pichon et al. 2011; Aumer, White & Naab 2014). We chose the K3s–yA–IaB–kB as a reference model to further investigate stellar ages in the galaxy disc. Comparable conclusions can be drawn also for other galaxy models with extended stellar discs: however, we preferred to overplot only one further radial profile in Fig. 6 for the sake of clarity. Also, restricted regions where inspecting the age of stars located in the disc have to take into account the galaxy morphology, so that it is not trivial to define only one region for all
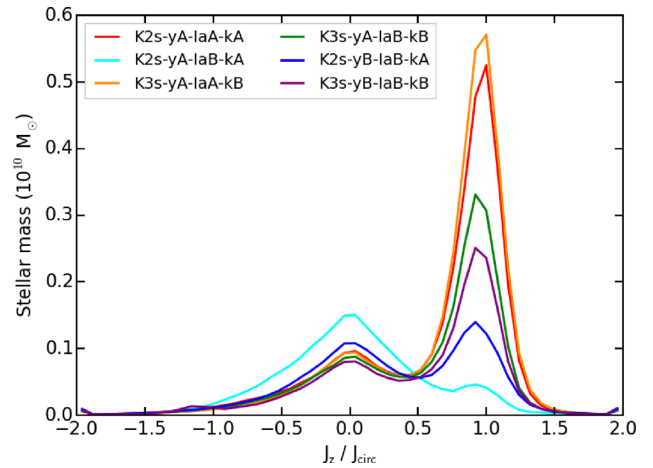
**Table 2.** Success of galaxy models in matching observational constraints considered throughout Section 4. Each row refers to a galaxy model of our simulation suite. Columns are the observational tests.

| Name | Dominant stellar disc component | SN Ia rates | SN II rates | Gas metallicity gradient | Stellar metallicity gradient | $\alpha$-enhancement pattern |
|------|------|------|------|------|------|------|
| K2s–yA–IaA–kA | ✓ | ✗ | ✓ | ✗ | ✓ | ✗ |
| K2s–yA–IaB–kA | ✗ | ✓ | ✓ | ✗ | ✓ | ✓ |
| K3s–yA–IaA–kB | ✓ | ✗ | ✓ | ✓ | ✓ | ✗ |
| K3s–yA–IaB–kB | ✓ | ✓ | ✓ | ✓ | ✓ | ✓ |
| K2s–yB–IaB–kA | ✗ | ✓ | ✓ | ✓ | ✓ | ✓ |
| K3s–yB–IaB–kB | ✓ | ✓ | ✓ | ✓ | ✗ | ✓ |
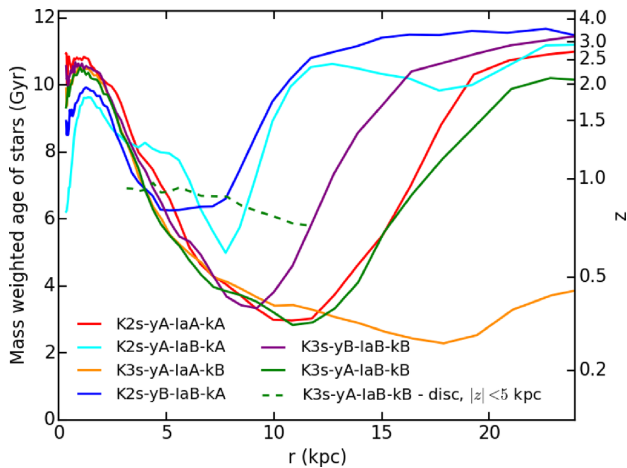


**Figure 6.** Radial profiles of the mass weighted age of stars within the galactic radii of the six simulations. For simulation K3s–yA–IaB–kB (green) we also show the mass weighted age of stars in the disc (dashed line).

(bottom right). Vertical lines show the median of each distribution and highlight the formation epoch of different components.

We then analyse SN rates in our set of simulated galaxies. Fig. 9 shows the redshift evolution of SN Ia (left-hand-side panel) and SN II (right-hand-side panel) rates, where rates are expressed as events per century and per $10^{10}\,M_\odot$. We compute rates as SN events between two simulation outputs over the time between the outputs. We compare predictions from our simulations with observations by Mannucci et al. (2005). These authors compute the rate of SNe for galaxies belonging to different morphological classes: here we consider SN Ia and SN II rates for galaxies classifies as irregular, S0a/b and Sbc/d in the observational sample. Error bars represent the $1\sigma$ error (including uncertainties on SN counts, and host galaxy magnitude and inclination), but do not account for uncertainties on the estimate of the mass for galaxies in the observational sample, which is quoted to affect measurements by ~40 per cent.

By comparing Figs 9 and 3, we can appreciate how SN II rates trace the evolution of the SFR. We find that SN II rates of our galaxies are in keeping with observations from late-type Sbc/d galaxies, the galaxy model K2S–yA–IaA–kA slightly exceeding them. Also, we find a good agreement between SN Ia rates of simulations adopting the lower fraction of binary systems that host SNIa and observations from Sbc/d galaxies. The comparison with Mannucci et al. (2005) data supports a value for the fraction of binary systems suitable to give rise to SNe Ia of 0.03, while disfavouring the value 0.1 (at least for late-type galaxies and when the IMFs that we are adopting are considered). Matching observational data of Mannucci et al. (2005) is a valuable result of our simulations: SN rates are indeed a by-product of the chemical

evolution network in our simulations, and reflect the past history of star formation and feedback of the galaxy (see also Table 2). Also, the comparison between computed SN rates with observations can be used as a powerful tool to predict or at least validate the morphological type of the simulated galaxies.

### 4.3 Metallicity profiles

#### 4.3.1 Stellar metallicity gradient

In this section we analyse stellar metalicity gradients of simulated galaxies and compare predictions from simulations to observations, taking advantage of the wealth of accurate measurements available for our Galaxy. Fig. 10 shows the iron abundance radial profile for the set of simulated galaxies. Results are compared with observations of Cepheids in MW from different authors (further detailed in the legend and caption of the figure). Here, and in Figs 11 and 12, we consider only those stars whose age is <100 Myr in simulated galaxies, since Cepheids are stars younger than ~100 Myr (Bono et al. 2005). Ages of young open clusters and star-forming regions in Spina et al. (2017) are younger than ~100 Myr, too (see Fig. 10). When different from ours, solar reference abundances adopted in the observational samples have been properly rescaled.

Fig. 11 shows the radial abundance gradient for oxygen. We compare predictions from our simulations with observations of Cepheids from Luck & Lambert (2011), according to the division in bins as a function of the Galactocentric distance computed by Mott, Spitoni & Matteucci (2013). Error bars indicate the standard deviation computed in each bin, that is 1 kpc wide.

Fig. 12 compares radial profiles for the abundance ratio [O/Fe] in simulations with observations of Cepheids (Luck & Lambert 2011; Mott et al. 2013). Observations show that stars in the disc of MW are not $\alpha$-enhanced, on average, with respect to solar values. Data of Mott et al. (2013) have been shifted by the authors themselves (by the following amounts: $-0.17$ dex for [O/H], $-0.07$ for [Fe/H]) with respect to the original data of Luck & Lambert (2011), due to the discrepancy of the dataset of Luck & Lambert (2011) with previous observations by the same authors (see below).

Negative radial abundance gradients are recovered for all the galaxies, thus in agreement with observations (Figs 10 and 11). The slope of the profiles (for distances from the galaxy centre larger than $r > 4$ kpc) is in keeping with observations, thus indicating the effectiveness of our sub-resolution model to properly describe the chemical enrichment of the galaxy at different positions.

Focusing on the normalization of oxygen profiles, comparison with Cepheids supports a K2s IMF. The K2s IMF leads to a fair agreement with observations also when the normalization of iron profiles is considered: however, in this case, a value of 0.1 for
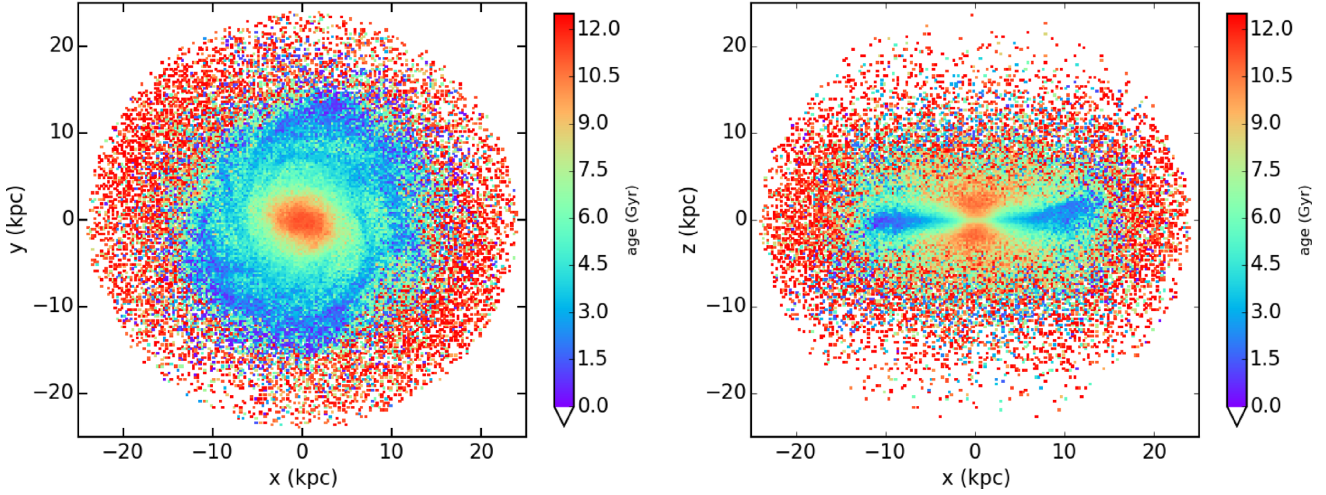
**Figure 7.** Face-on (left-hand panel) and edge-on (right-hand panel) binned distributions of all the star particles located within the galactic radius for the K3s–yA–IaB–kB (green) simulation. Plots are shown at redshift $z = 0$; the colour encodes the mean age of the star particles in the bin.
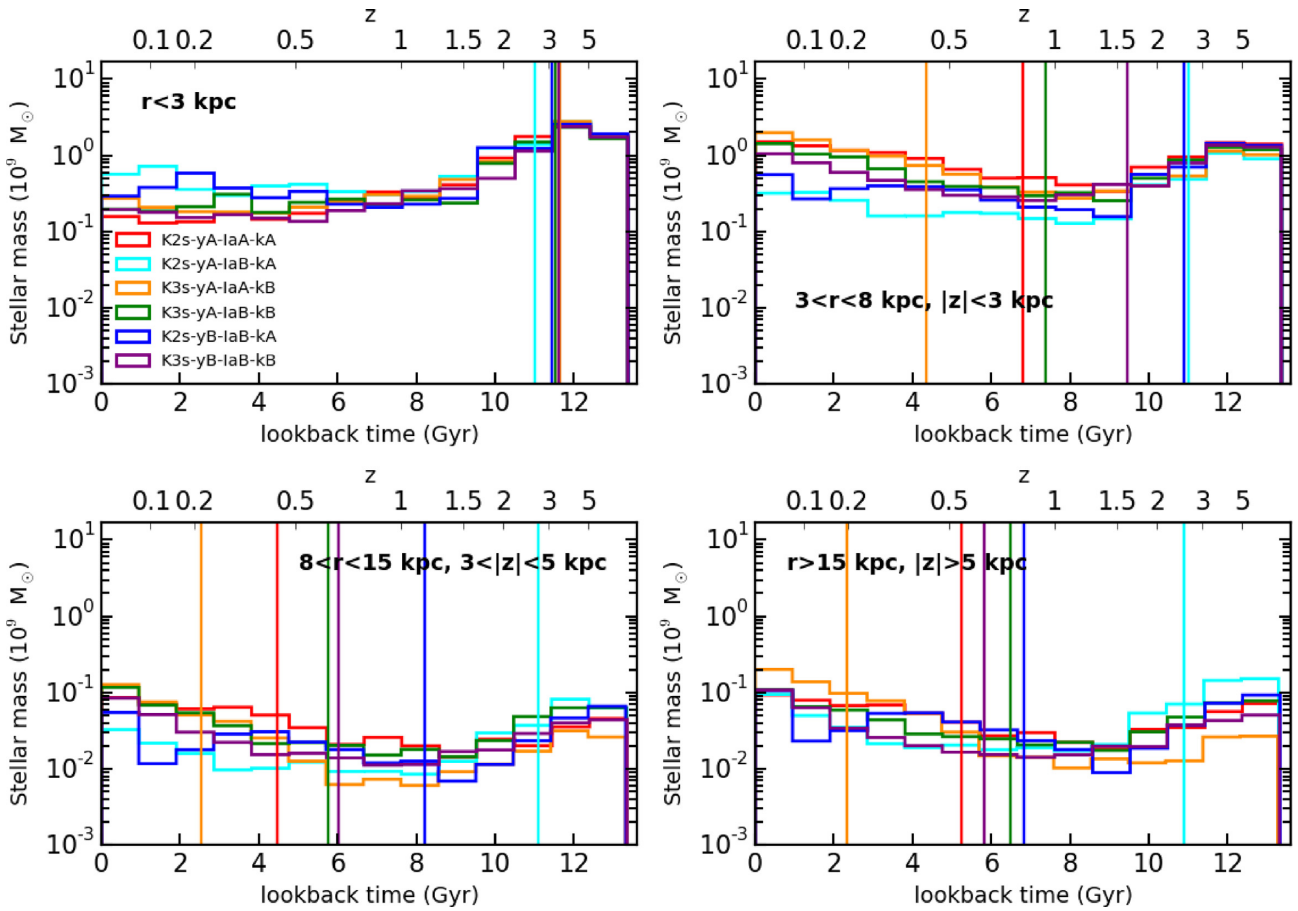


**Figure 8.** Distribution of stellar mass per bin of lookback time for all the simulations. The four panels consider different regions of the volume $r < R_{gal}$, as reported in each panel, and roughly identify the following components of the galaxy: bulge (top left), inner disc (top right), outer disc (bottom left), and halo (bottom right). Vertical lines show the median of each distribution, and highlight the formation epoch of different component.

the fraction of binary systems with characteristics suitable to host SNe Ia is the driver for matching observations. Indeed, when the value of 0.03 is considered, the amount of iron produced is not enough to agree with data. The set B of stellar yields lowers the

normalization of metallicity gradients, as a lower amount of oxygen and iron are synthesized (see Section 4.6). Iron profiles in galaxies simulated adopting this set of yields underestimate observations by $\gtrsim 0.5$ dex (Fig. 10). Also, there exists a degeneracy between the
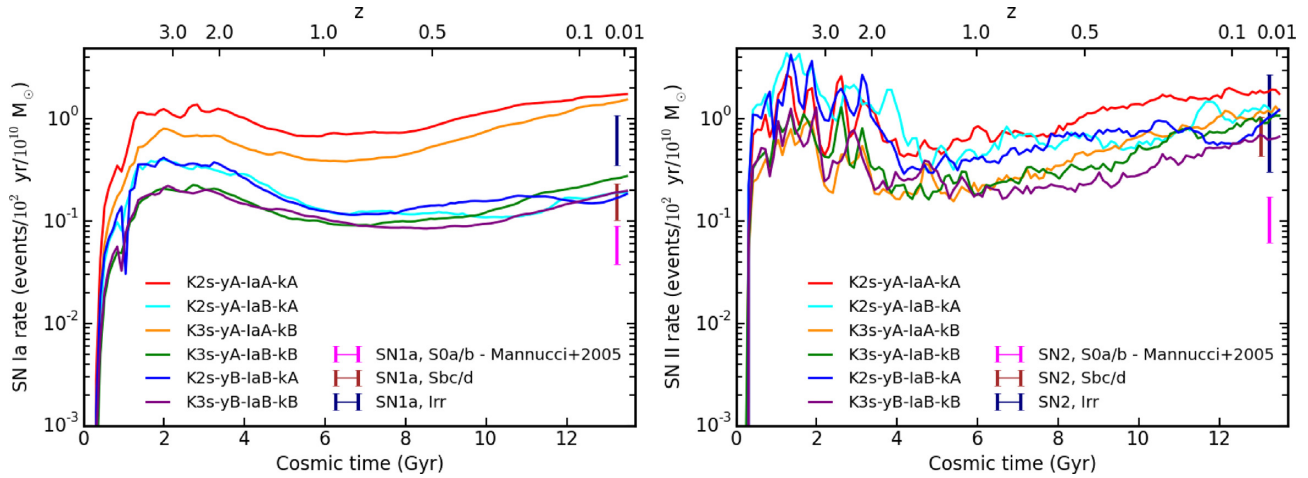
**Figure 9.** Evolution of SN Ia (left-hand-side panel) and SN II (right-hand-side panel) rates for the simulated galaxies. Rates are expressed as events per century and per $10^{10}$ M$_\odot$. Our predictions are compared with observations by Mannucci et al. (2005) for local universe galaxies with different morphological type, as highlighted in the legend.
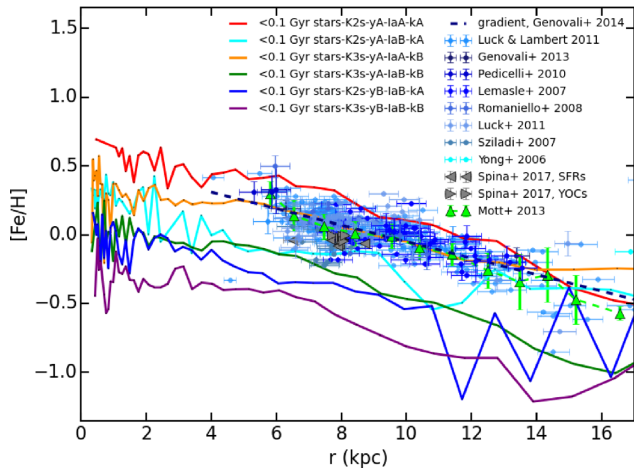


**Figure 10.** Iron abundance radial profile for young stars in the simulated galaxies (colours as in the legend and previous figures). We compare results with observations of Cepheids in the catalogue of Genovali et al. (2014a), which include data from Yong et al. (2006), Lemasle et al. (2007), Sziládi et al. (2007), Romaniello et al. (2008), Pedicelli et al. (2010), Luck et al. (2011), Luck & Lambert (2011), and Genovali et al. (2013). Dashed blue line depicts the metallicity gradient for the whole sample (Genovali et al. 2014b). We also consider data for young open clusters (YOCs) and star-forming regions (SFRs) in MW from Spina et al. (2017). Green symbols highlight observations of Luck & Lambert (2011) according to the binning by Mott et al. (2013).
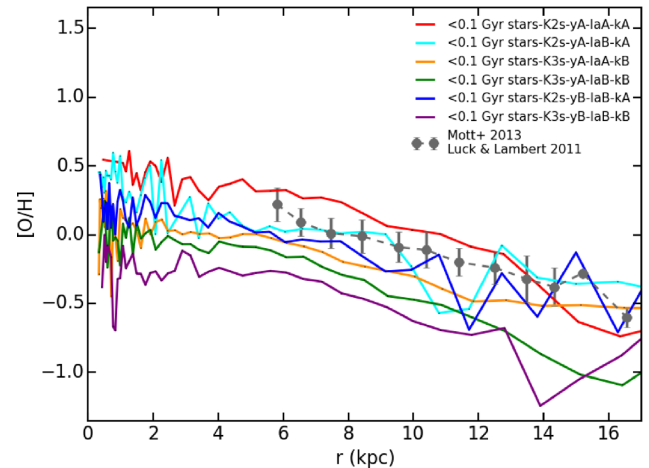
adopted IMF and the set of yields, the galaxy models K3s–yA–IaB–kB and K2s–yB–IaB–kA providing comparable results. Peaks at distances $r > 10$ kpc for galaxies K2s–yA–IaB–kA and K2s–yB–IaB–kA are due to the reduced amount of stars as the outermost regions of the stellar disc are reached.

Figs 10 and 11 suggest that young stars in these simulated galaxies are more metal poor than observed ones in MW, when both the iron and the overall metal content (approximately oxygen) are considered. This is especially true for those models of galaxies that best-fitting the observations of gas oxygen abundance profiles

**Figure 11.** Oxygen abundance radial profile for young stars in the set of galaxies. Data show the radial gradient for oxygen from observations of Cepheids (Luck & Lambert 2011), according to the division in bins computed by Mott et al. (2013). Error bars show the standard deviation in each bin.

in Fig. 13 (see Section 4.3.2), and in particular for K3s–yA–IaB–kB (green). A possible reason for that stems from the star formation history of our galaxies. MW-like galaxies often assemble a considerable part of the stellar mass in the disc in the redshift range $2.5 \lesssim z \lesssim 1$ (van Dokkum et al. 2013; Snaith et al. 2014). Our galaxies are instead characterized by a quiescent star formation in the redshift range $2 \lesssim z \lesssim 1$, as shown in Fig. 3. Should a more continuous and sustained star formation at $2.5 \lesssim z \lesssim 1$ occur, a higher quantity of metals is produced and provided to the ISM, so that stars born after $z \sim 1$ would be much metal richer than they actually are.

However, we would like to emphasize two relevant aspects that cannot be neglected and that could alleviate the tension between our predictions and observations. These are the uncertainties that affect metallicity determinations in observations and the peculiarity of Cepheids.
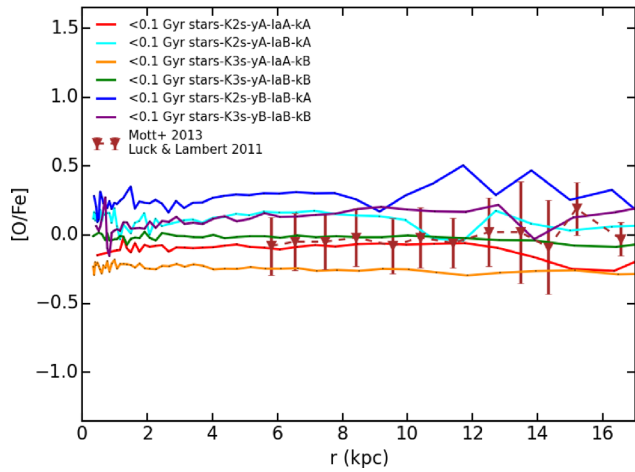
**Figure 12.** Oxygen-over-iron abundance profile for young stars in simulated galaxies. Observations of Cepheids from Luck & Lambert (2011), according to the binning performed by Mott et al. (2013).
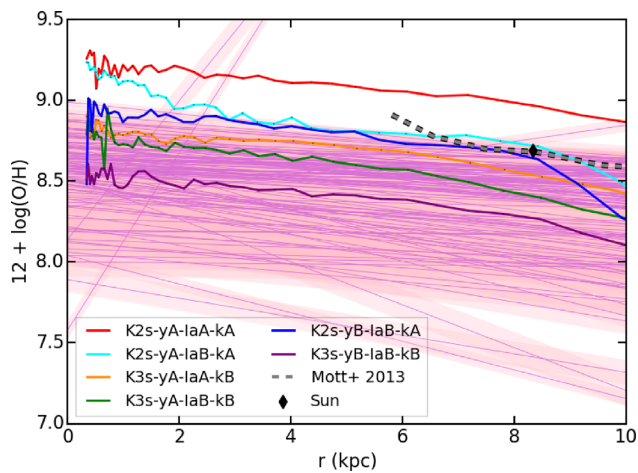


**Figure 13.** Oxygen abundance radial profile for gas in the simulated galaxies (colours as in the legend and previous figures). Light-blue profiles are observed metallicity gradients from the sample of 130 nearby late-type galaxies of Pilyugin et al. (2014). The shaded envelope around each profile depicts the scatter of oxygen abundance around the trend. We also show the metallicity gradient of MW (dashed curve) as deduced from observations of young stars in our Galaxy, and the position of the Sun on the plane (see the text for details).

First, abundance estimate reliability is a delicate topic, as different sources of error enter final determinations (see e.g. Luck & Lambert 2011). The quoted typical uncertainties for values of [Fe/H] in Cepheids catalogues considered in Fig. 10 are 0.1 dex (Romaniello et al. 2008) or 0.2 dex (Yong et al. 2006). Also, Luck & Lambert (2011) found a discrepancy of 0.07 dex between the [Fe/H] derived from their sample and that computed for common objects in previous works by Luck, Kovtyukh & Andrievsky (2006) and Luck et al. (2011). In these works they used equivalent analysis techniques, eventually tracing back to the changed surface gravity of stars the most plausible reason of the mismatch (see the discussion in section 4.1.1 of Luck & Lambert 2011, for further details). The discrepancy was even larger (∼0.17 dex) when [O/H] is taken into account. Besides, variability of Cepheids can enter final estimates that can suffer an uncertainty as high as ∼0.1 dex due to the observed phase (Luck & Lambert 2011).

Also, different procedures adopted for metallicity calibrations yield remarkably different results. For instance, Kewley & Ellison (2008) quantified that different techniques aimed at determining abundances from metallicity-sensitive emission-line ratios affect the normalization of profiles by up to 0.7 dex. This, along with parameters in the sub-resolution physics that enter the modeling of the chemical enrichment process in simulations, usually leads different authors not to consider at all the normalization of the metallicity profiles or of the mass–metallicity relation. They rather focus on slopes only and, in case, on the evolution of the normalization of metallicity profiles (e.g. Torrey et al. 2017). Therefore, differences in the normalization of profiles by up to few tens of dex should not be considered as indicative of a serious disagreement between predictions from simulations and observations.

The second aspect concerns the possibility that Cepheids are stars with a metal content that is, on average, higher than what usually observed in nearby disc galaxies. This issue will be thoroughly addressed in Section 4.3.2.

### 4.3.2 Gas metallicity gradient

We continue our analysis by further investigating the metal content of gas in our galaxies. Fig. 13 shows the gas metal content of simulated galaxies. We analyse oxygen abundance gradients, oxygen being one of the most accurate tracers of the total metallicity. We compare results from our set of simulations with the oxygen abundance radial profiles of the 130 disc galaxies that make up the observational sample of Pilyugin, Grebel & Kniazev (2014). The gas metal content of these late-type galaxies in the local universe has been inferred from spectra of H II regions. Since we are not simulating our Galaxy, the comparison with properties of a set of disc galaxies is a key test.

All the simulated galaxies are characterized by negative gradients, in agreement with the majority of observed galaxies and with the scenario that outer regions of the galaxy discs are younger than inner ones (see also Section 4.2). Also, the slope of profiles of simulated galaxies is in keeping with the bulk of observations: this feature highlights the ability of our sub-resolution model to describe properly the local chemical enrichment process, as well as the circulation of metals driven by galactic outflows.

As for the amount of oxygen in the gas (i.e. the normalization of profiles), we find that the K2s IMF overproduces massive-star related metals. The oxygen profile of the galaxy K2s–yA–IaA–kA lies ∼0.3 dex above the highest observed metallicity gradients, and the K2s–yB–IaB–kA model traces the upper edge of the observed metallicity range (see also below). On the other hand, we see that assuming the K3s IMF leads to a better agreement with observations by Pilyugin et al. (2014). The K3s IMF limits the number of massive stars, thus resulting in a lower amount of massive-star-related metals produced and provided to the ISM.

The set B of stellar yields drifts towards a better agreement with observations (compare, for instance, K2s–yB–IaB–kA and K3s–yB–IaB–kB models with K2s–yA–IaA–kA and K3s–yA–IaB–kB ones, respectively), as a lower amount of oxygen is produced. This result is more striking when contrasting the green and purple galaxies that experience similar star formation histories.

An interesting indication of our analysis is that a Kroupa et al. (1993) (K3s) IMF leads to a better agreement with metallicity profiles of late-type galaxies in the nearby universe shown in Fig. 13.

The comparison with the sample of Pilyugin et al. (2014) suggests that an IMF more top-light than Kroupa (2001) (K2s) and Chabrier (2003) has to be preferred for local disc galaxies.

However, the scenario becomes puzzling and the interpretation of results more challenging when we consider metallicity determinations for MW along with measurements in the sample of Pilyugin et al. (2014). We overplot in Fig. 13 the oxygen abundance gradient of Cepheids in MW by Mott et al. (2013, see the dashed grey line in Fig. 11). Considering that the metal content of stars reflects directly that of gas out of which they formed, the metal content of young stars should be comparable to that of gas at redshift $z = 0$, or should fall slightly below, at most. Also, we show where the Sun is located in Fig. 13, considering $R_\odot = 8.33$ kpc as the distance of the Sun from the Galaxy centre (Bovy, Hogg & Rix 2009; Gillessen et al. 2009), and $\log_{10} \varepsilon_O = 12 + \log_{10}(O/H)_\odot = 8.69$ (Asplund et al. 2009). We see that the metal content of young stars in MW (that is a lower limit for the gas metallicity) outlines the extreme upper edge of the region where observations by Pilyugin et al. (2014) locate.

This points out that either there are some issues with calibrations of metallicities in the considered observational samples, or Cepheids are stars with a metal content that is, on average, higher than what usually observed in nearby disc galaxies. If we deem the metallicity estimates of both samples as reliable, then we can conclude that the K2s IMF is more suitable for MW, while a K3s IMF should be preferred for other disc galaxies in the local universe.

Also, it is striking that the Sun is characterized by an oxygen abundance comparable to that of Cepheids at the same distance from the Galaxy centre, although it is by far older than them. We envisage that the availability of more accurate observational determinations in the near future will alleviate the tension between discordant results and corroborate more robust conclusions. In Section 4.5 we further discuss how metals are retained and distributed in and around galaxies.

### 4.4 Stellar $\alpha$-enhancement

We further analyse the metal content of the stellar component of our galaxies focusing on the stellar enhancement in $\alpha$-elements with respect to the solar ratio. Fig. 14 shows [O/Fe] ratios as a function of [Fe/H] for the set of simulated galaxies. Each row refers to a galaxy model. Panels of the left-hand column represent the distribution of all the star particles in the volume we are analysing ($r < R_{gal}$; see Section 4.1). Central and right-hand columns show the distribution [O/Fe] ratios versus [Fe/H] for two subsamples of star particles, representative of stars located in the bulge and in the disc of galaxies, respectively.

We sliced the whole sample of star particles according to the kinematic diagnostic indicator $J_z/J_{circ}$ (see Section 4.1). We selected star particles with $-0.1 < J_z/J_{circ} < 0.1$ as belonging to the bulge, and star particles with $0.9 < J_z/J_{circ} < 1.1$ as located in the galaxy disc. Then, we also verified the position of selected particles, restricting the bulge subsample to star particles located at $r < 3$ kpc from the galaxy centre, and the disc subsample to star particles whose distance from the galaxy centre is $3 < r < 13$ kpc and whose galactic latitude is $|z| < 5$ kpc (as done in Fig. 6, for instance). The number of star particles considered in second- and third-column panels of Fig. 14 is not always the same, as galaxies have different stellar mass in the disc and the bulge (see Fig. 5).

Particles selected according to these criteria sample-specific components of the galaxy: their chemical features will be compared to observed stars that are located in the bulge or the disc of MW and that are characterized by peculiar evolutionary patterns.

Predictions from our simulated galaxies are compared with the following observational data set: (i) Meléndez et al. (2008): they observed bulge, halo, thin and thick[4] disc giant stars; the quoted uncertainties of their data are 0.03 dex in *Fe* and 0.1 dex in [O/Fe]. (ii) Cayrel et al. (2004): they investigated very metal-poor halo giant stars, and state that the error in their abundance estimates can be as large as $\sim$0.2 dex. (iii) Edvardsson et al. (1993): they observed dwarf stars in the disc of MW; quoted errors are 0.1 dex for abundances relative to hydrogen, and uncertainties comparable or even smaller for abundances relative to iron. In second- and third-column panels we only consider observations for stars in the bulge or disc, respectively.

When different from ours, solar reference abundances adopted in the observational samples have been properly rescaled and homogenized.

The background two-dimensional histograms in Fig. 14 consider the distribution of star particles in the plane [O/Fe] versus [Fe/H]. We compare results from simulations to observations of single stars under the assumption that the metal content of a star particle in simulations statistically reproduces the mean metallicity of the SSP that the star particle samples. We refer the reader to Valentini et al. (2018) for another possible method (see also Grand et al. 2018a).

General trends that we observe by investigating results shown in Fig. 14 and comparing galaxy models are the following. Adopting the K3s IMF leads to an overall reduction of oxygen that is in contrast with observations of stars in MW. This is strikingly evident when contrasting results from K2s–yA–IaA–kA (first row) and from K3s–yA–IaA–kB (third row). Decreasing the number of systems suitable for hosting SNe Ia does not shift the bulk of star particles towards values of [O/Fe] high enough to alleviate the tension.

As for the fraction of binary systems originating SNe Ia, the comparison with observations in Fig. 14 definitively rules out the value 0.1, as it produces an excess of stars with low [O/Fe] and super-solar [Fe/H] that is not in keeping with observations.

A result that emerges from this analysis is that stellar yields affect the cooling process and are therefore a key driver of star formation, especially at high redshift. As a consequence, changing the adopted set of yields shapes directly the patterns of chemical evolution and stellar $\alpha$-enhancement. Two main features appear when the set B of stellar yields is adopted, regardless of the considered IMF: (i) a lower amount of iron is produced (see Section 4.6), and (ii) the galaxy bulge is more $\alpha$-enhanced and forms over shorter time-scales. By comparing second and fifth rows in Fig. 14, we see that the bulk of stellar mass in the bulge of K2s–yB–IaB–kA (blue model) forms at earlier epochs (i.e. lower [Fe/H]) than K2s–yA–IaB–kA (cyan model), as also highlighted in the first panel of Fig. 8. Also, it has been highly enriched by the chemical feedback from massive stars (see below). A similar picture holds when K3s–yA–IaB–kB and K3s–yB–IaB–kB are considered, too.

The set B of stellar yields allows to obtain the best agreement with observations, especially when the K2s IMF is assumed (fifth row of Fig. 14). Results for the galaxy model K2s–yB–IaB–kA are in remarkable agreement with data: we find that stars in the bulge have [O/Fe] that span from typical values of halo stars ([O/Fe] $\sim 0.4-0.6$) to slightly sub-solar values as the iron abundance

---

[4]Given the resolution of our simulations, we do not attempt to resolve the structure of the simulated galaxy disc by distinguishing between thick and thin disc.
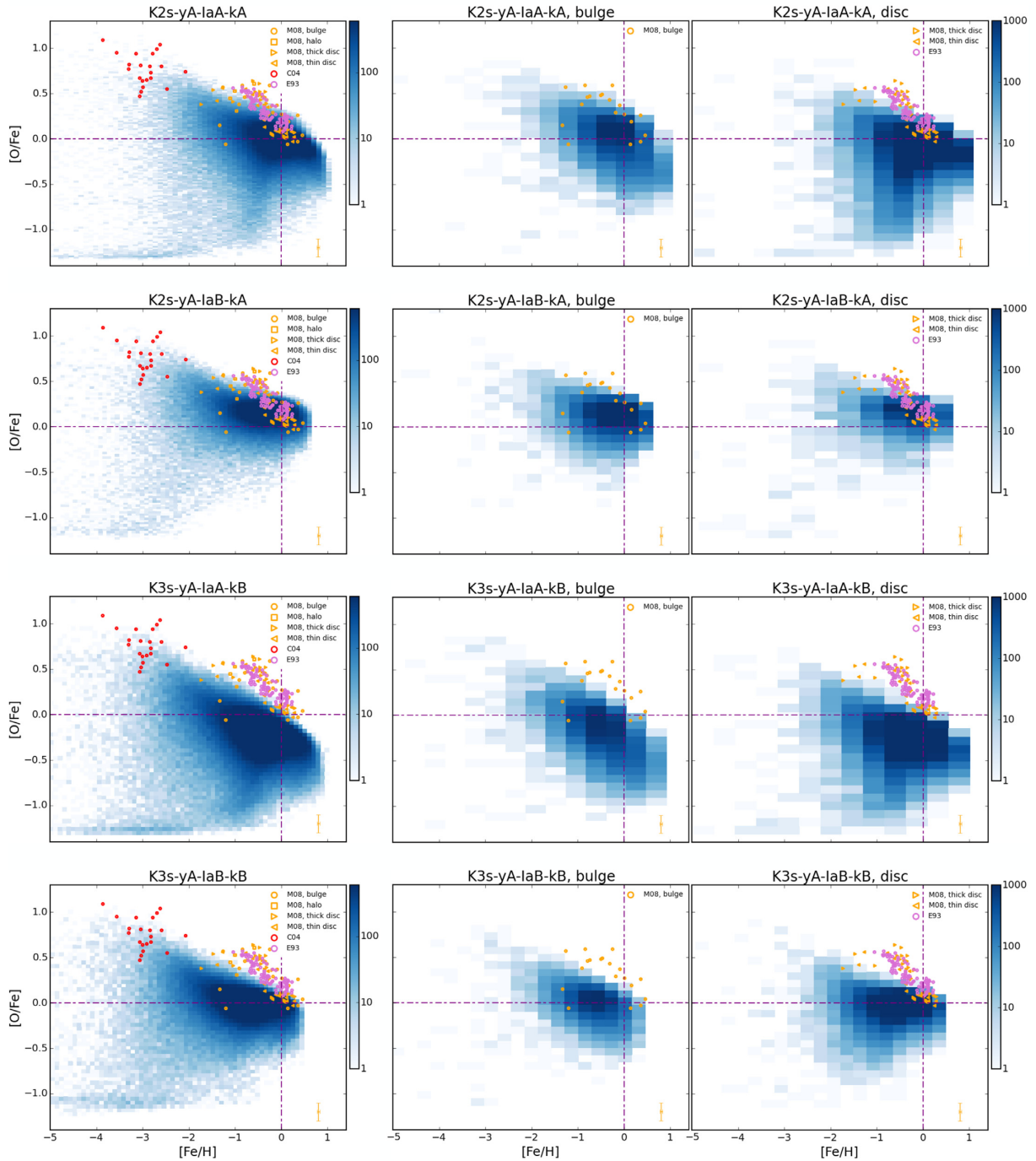
**Figure 14.** [O/Fe] as a function of [Fe/H] for star particles in our simulations, at $z = 0$. Each row corresponds to a galaxy model. We show the [O/Fe] versus [Fe/H] for all the star particles within $R_{gal}$ (left-hand column), for star particles belonging to the bulge (centre), and for star particles in the disc (right-hand column). Each colour bar encodes the number of star particles per pixel. We contrast our results with observations of Meléndez et al. (2008, M08), of Cayrel et al. (2004, C04), and of disc stars by Edvardsson et al. (1993, E93). Dash-dotted violet lines highlight solar values. A representative error bar for Meléndez et al. (2008, M08) data is shown.

approaches [Fe/H] = 0. This trend is in keeping with findings by Zoccali et al. (2006) and Meléndez et al. (2008). Also, the location of the break at [Fe/H] $\sim -1 - -0.5$ is in agreement with observations. Bulge stars that shape this break highlight that the formation of the bulge occurred over a time longer than $\sim 1$ Gyr, so that SN Ia contributed with iron to the enrichment of the ISM.

This feature is remarkably evident when the set B of stellar yields is adopted, while the transition to the regime where SN Ia contribute to the enrichment is smoother for the set A. The bulk of stars in the disc with [Fe/H]$\gtrsim -0.5$ are characterized, on average, by a lower $\alpha$-enhancement with respect to stars in the bulge. This is in agreement with the scenario according to which the formation
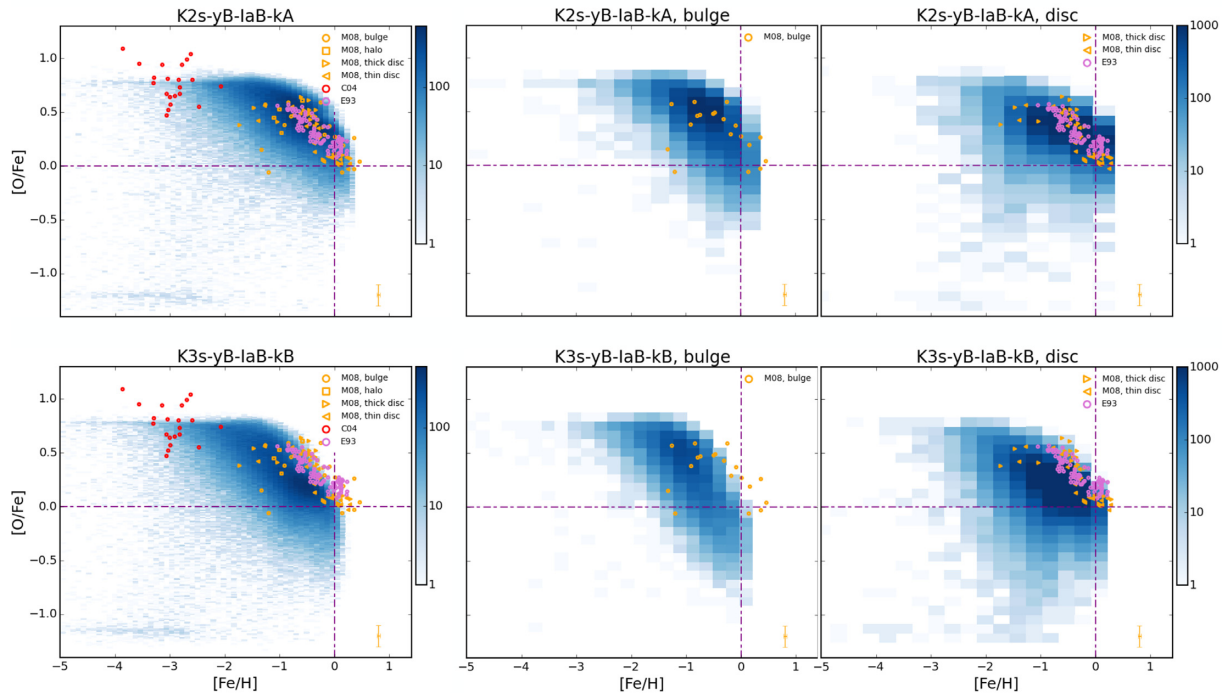
**Figure 14.** *–continued*

of the disc in late-type galaxies occurs over longer time-scales than the bulge component, that is conversely mainly affected by early feedback from massive stars (see e.g. Lecureur et al. 2007). However, observed stars belonging to the bulge or to the disc of MW do not occupy distinct regions in the [O/Fe]–[Fe/H] plane, they rather overlap for almost all the considered values of [Fe/H] (see e.g. Meléndez et al. 2008). Adopting the set B of stellar yields also reduces the number of star particles characterized by sub-solar values of both [O/Fe] and [Fe/H], which do not have an observational counterpart.[5]

Few et al. (2014) explored the impact of the adopted IMF and binary fraction on the chemical evolution of a disc galaxy having a virial mass approximately half of that of our galaxies. Interestingly, they found that the slope of the [O/Fe]–[Fe/H] relation for stars characterized by [Fe/H] $\gtrsim -1$ is regulated by the value of the binary fraction, and that the more top-heavy Kroupa (2001) IMF produces [O/Fe] larger by ∼0.2 dex with respect to the Kroupa et al. (1993) IMF, in keeping with our results.

Fig. 15 further investigates the stellar $\alpha$-enhancement focusing on the [Mg/Fe] ratios as a function of [Fe/H], for three galaxies selected out of the set. We contrast our results with observations of the AMBRE project (de Laverny et al. 2013; Mikolaitis et al. 2017), and of disc stars by Edvardsson et al. (1993). Trends observed and discussed for the stellar [O/Fe] versus [Fe/H] relation in Fig. 14 are confirmed. Once again, we find a remarkable agreement with observations for the galaxy model K2s–yB–IaB–kA.

Results in this section show a better agreement with observations of stars in our Galaxy when the K2s IMF is assumed. On the other hand, the comparison of gas metallicity profiles with observations

of a sample of disc galaxies in the local universe (Section 4.3.2) strongly supports the K3s IMF. Therefore, in agreement with our previous findings in Section 4.3.1, we predict that MW stars exhibit a higher metal content with respect to other nearby late-type galaxies. Interestingly, stars of MW are found to be more $\alpha$-enhanced than stars in nearby dwarf galaxies, and not representative of stellar populations in dwarfs (Venn et al. 2004, and references therein), even if different formation scenarios can enter this result.

We stress once again that our goal is not to reproduce observations of the MW and that we simulate a disc galaxy that should not be considered as a model for the MW. We are rather interested in investigating whether an accurate and controlled model of chemical evolution as the one we adopt in our simulations is able to yield chemical evolutionary patterns that are associated with specific components and time-scales by observations.

### 4.5 Metals in and around galaxies

In this section we focus on the spatial distribution of metals in and around galaxies as the result of chemical feedback from outflows. Comparing predictions from our simulations with observations of the CGM is beyond the scope of this paper, as this kind of analysis would require an accurate modelling of the ionization state of the gas. Here we want to show that the high galactic metal content reached when the K2s IMF is assumed (see Fig. 13) is not due to the ineffectiveness of galactic outflows in removing metals from sites of star formation, within the innermost regions of galaxies. To pursue that, we analyse how the mass budget of metals is distributed at an increasing distance from the galaxy centre.

Fig. 16 shows the cumulative distribution of metals in gas and stars of simulated galaxies as a function of the distance from the galaxy centre. We consider 3 Mpc as the outermost distance within which to compute the mass of metals as this is the radius of the

---

[5]The lack of an observational counterpart may be ascribed to the fact that these stars are rather rare. These results can be considered predictions from our simulations.
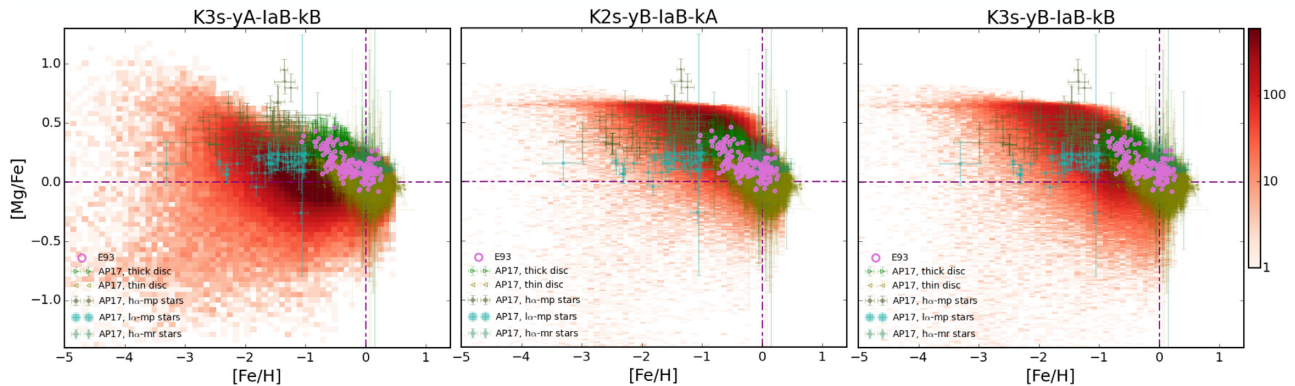
**Figure 15.** [Mg/Fe] as a function of [Fe/H] for star particles in three simulations, at $z = 0$. Each panel corresponds to a galaxy model (green, blue, and purple from left to right). We show the [Mg/Fe] versus [Fe/H] for all the star particles within $R_{gal}$. Each colour bar encodes the number of star particles per pixel. Results are compared with observations of the AMBRE project (Mikolaitis et al. 2017, AP17), and of disc stars by Edvardsson et al. (1993, E93). Dash-dotted violet lines highlight solar values. Data from the AMBRE project are split into thick and thin disc stars, high- and low-$\alpha$ metal-poor population, and high-$\alpha$ metal-rich population. They are provided with error bars.
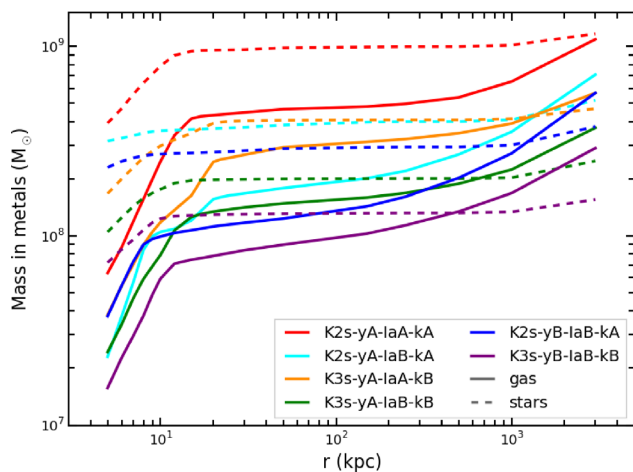


**Figure 16.** Cumulative radial distribution of metals in gas (solid lines) and stars (dashed lines) in our simulated galaxies. Each curve shows the mass of metals in gas and stars enclosed within a given distance from the galaxy centre.

largest sphere that can be contained in the volume with high-resolution particles (see Section 2.1).

Metals have been produced by stars in the main galaxy sitting at the centre of the simulated halo and by stars in satellites and few small field galaxies. The latter stars are responsible for the mild increase of the mass of metals in stars at distances larger than the galactic radius ($R_{gal} \simeq 24$ kpc) of the main galaxies. Radial profiles of mass of metals in stars in Fig. 16 smoothly increase up to reach the stellar extent of galaxies, and then marginally rise when other stars not associated with the main galaxies are met in the volume.

Radial distribution of metals in gas show how galactic outflows are effective in driving metals outwards from star-forming regions in galaxies and in promoting the metal enrichment of the ISM and CGM. The mass of metals in gas rapidly increases in the ISM of the galaxy up to distances $r \simeq 20$ kpc; from there outwards the mass of metals in gas increases by up to a factor $\sim 2-3$. Outside $R_{gal}$ metals are retained by the diffuse CGM. We find that the mass of metals in gas within a distance of 20 kpc from the galaxy centre is $18 \pm 4$ per cent of the total amount of metals produced (within 3

Mpc[6]) and $31 \pm 9$ per cent of the metals produced that belong to the gaseous phase. Metals in gas and stars within 20 kpc account for at least $\sim 40$ per cent of the metals produced within 3 Mpc. The mass of metals in gas and stars within 150 kpc from the galaxy centre constitutes $57 \pm 9$ per cent of the metals produced. This result is in remarkable agreement with Peeples et al. (2014), which investigated a sample of nearby star-forming galaxies with stellar mass in the range $10^9 - 10^{11.5}$ M$_\odot$ and found that galaxies retain $\sim 50$ per cent of produced metals in their ISM/CGM and stars out to 150 kpc, with no significant dependence on the galaxy mass.

By analysing the mass distribution of metals in gas and stars of our galaxies, we find the following results. The mass of metals locked in stars within 10 kpc from the galaxy centre is at least twice as high as that in gas (mass ratios range between 2.22 and 3.42). The mean star-over-gas metal mass ratio 20 kpc far from the galaxy centre is $1.96 \pm 0.40$, while at 50 kpc it is $1.80 \pm 0.41$. A minimum distance of $\sim 500$ kpc (i.e. beyond the galaxy virial radius) has to be reached in order to have a comparable mass of metals retained by stars in the galaxy and present in the ISM and CGM of the galaxy. Table 3 summarizes relevant quantities of the simulated galaxies.

Also, the radial distribution of metals in gas shown in Fig. 16 sheds further light on the metal content of gas within the galaxies shown in Fig. 13. Galaxy models assuming the K2s IMF are characterized by an oxygen abundance of gas that is higher than commonly observed in disc galaxies in the local universe. This feature cannot be ascribed to the inability of galactic outflows to drive metals outward from sites of star formation within the galaxy. Conversely, outflows in galaxies adopting the K2s IMF are as effective as those in models with the K3s IMF, but an overproduction of metals occurs when the K2s IMF is assumed (see Section 4.3.2). Thus, our prediction that a Kroupa et al. (1993) IMF seems to be preferred when dealing with nearby late-type galaxies is further corroborated.

### 4.6 Stellar yields

In this section we quantify the impact of the adopted set of stellar yields. We analyse the mass of oxygen and iron that is produced by

---

[6]We are therefore quoting upper limits.

**Table 3.** Relevant quantities of the simulated galaxies. Column 1: simulation label. Column 2: virial radius. Note that the galactic radius $R_{\rm gal} = 0.1\, R_{\rm vir}$. Column 3: ratio between gas mass and gas plus stellar mass within $R_{\rm vir}$. Column 4: mass of metals in gas over gas plus stellar mass within $R_{\rm vir}$. Column 5: mass of metals in stars over gas plus stellar mass within $R_{\rm vir}$. Column 6: ratio between gas mass and gas plus stellar mass within $R_{\rm gal}$. Column 7: mass of metals in gas over gas plus stellar mass within $R_{\rm gal}$. Column 8: mass of metals in stars over gas plus stellar mass within $R_{\rm gal}$.

| Name | $R_{\rm vir}$ (kpc) | $\dfrac{M_{\rm gas}}{M_{\rm gas+stars}}$ | $\dfrac{M_{Z,\rm gas}}{M_{\rm gas+stars}}$ | $\dfrac{M_{Z,\rm stars}}{M_{\rm gas+stars}}$ | $\dfrac{M_{\rm gas}}{M_{\rm gas+stars}}$ | $\dfrac{M_{Z,\rm gas}}{M_{\rm gas+stars}}$ | $\dfrac{M_{Z,\rm stars}}{M_{\rm gas+stars}}$ |
|---|---|---|---|---|---|---|---|
| | | | Within $R_{\rm vir}$ | | | Within $R_{\rm gal}$ | |
| K2s–yA–IaA–kA | 238.7 | 0.77 | $2.8 \times 10^{-3}$ | $5.6 \times 10^{-3}$ | 0.37 | $7.6 \times 10^{-3}$ | $1.7 \times 10^{-2}$ |
| K2s–yA–IaB–kA | 236.8 | 0.84 | $1.4 \times 10^{-3}$ | $2.6 \times 10^{-3}$ | 0.39 | $4.9 \times 10^{-3}$ | $1.1 \times 10^{-2}$ |
| K3s–yA–IaA–kB | 241.5 | 0.81 | $1.5 \times 10^{-3}$ | $1.9 \times 10^{-3}$ | 0.42 | $3.9 \times 10^{-3}$ | $6.0 \times 10^{-3}$ |
| K3s–yA–IaB–kB | 240.3 | 0.85 | $8.3 \times 10^{-4}$ | $9.9 \times 10^{-4}$ | 0.47 | $2.7 \times 10^{-3}$ | $3.9 \times 10^{-3}$ |
| K2s–yB–IaB–kA | 236.9 | 0.84 | $1.1 \times 10^{-3}$ | $1.9 \times 10^{-3}$ | 0.33 | $3.7 \times 10^{-3}$ | $8.9 \times 10^{-3}$ |
| K3s–yB–IaB–kB | 239.6 | 0.87 | $5.8 \times 10^{-4}$ | $6.9 \times 10^{-4}$ | 0.47 | $2.0 \times 10^{-3}$ | $3.2 \times 10^{-3}$ |

an SSP according to the two different yield tables, once an IMF is assumed. We consider the K3s IMF in this section.

Fig. 17 shows the normalized cumulative mass in oxygen (left-hand panel) and iron (right-hand panel) that is produced by an SSP as a function of the mass of stars in the SSP. We consider newly produced elements for three values of the SSP metallicity $Z$: $2 \times 10^{-5}$, $1.2 \times 10^{-3}$, and $2 \times 10^{-2}$. The mass range spans between the minimum mass of the K3s IMF, that is 0.1 and 40 M$_\odot$ (see Section 2.3). In each panel, solid curves identify the set A of stellar yields, and dashed curves pinpoint the set B. As for the normalization, each curve is normalized to the maximum of the curve of that metallicity referred to the set A. In this way, it is possible to appreciate which set of yields predicts a larger amount of the considered element, at a given abundance.

Considering a star of a given mass, these figures describe the cumulative mass of an element (oxygen or iron) that is produced by stars with mass equal to or larger than the considered one. For instance, stars more massive than 15 M$_\odot$ and with a roughly solar metallicity $Z = 2 \times 10^{-2}$ have produced ∼55 per cent of the oxygen that has been synthesized, when the set A is considered.

The effect of changing yields on the metals produced by stars of different mass and initial metallicity is evident: different amounts of heavy elements are produced and this has significant consequences on the gas cooling and subsequent star formation. The lower the metal budget, the lower the cooling rate and the SFR, as discussed in Section 4.1.[7] When the set B of stellar yields is adopted, a lower amount of iron is produced for all the considered metallicities. The mass of synthesized oxygen is lower than that in the set A for SSPs with solar abundance, and slightly higher for lower values of $Z$. However, we note that the bulk of young stars are characterized, on average, by a roughly solar metallicity (see Fig. 11): as a consequence, also a lower amount of oxygen is produced when the set B is adopted, at least at low redshift. Total masses of oxygen and iron produced by SSPs with increasing metallicity increase when the set A of yields is adopted. When considering the set B of stellar yields, the total mass of iron keeps almost unaltered as a function of the metallicity $Z$, while the cumulative mass of oxygen slightly decreases as the metallicity increases.

## 5 DISCUSSION AND CONCLUSIONS

In this work we carried out a set of cosmological hydrodynamical simulations of disc galaxies, with zoomed-in ICs leading to the

formation of a halo of mass $M_{\rm halo,\,DM} \simeq 2 \cdot 10^{12}$ M$_\odot$ at redshift $z = 0$. These simulations have been designed to investigate the distribution of metals in galaxies and to quantify the effect of (i) the assumed IMF, (ii) the adopted stellar yields, and (iii) the impact of binary systems originating SNe Ia on the process of chemical enrichment. We considered either a Kroupa et al. (1993, K3s) or a Kroupa (2001, K2S) IMF, either a value 0.1 or 0.03 for the fraction of binary systems suitable to give rise to SNe Ia, and two sets of stellar yields.

The most relevant results of our study can be summarized as follows.

(i) We examined stellar ages and naturally predict that star formation in the disc always takes place later than in the bulge, and the disc formation proceeds inside-out.

(ii) We evaluated the evolution of SN rates in the set of simulated galaxies and compared them to observations of Mannucci et al. (2005). We find that SN II rates of our galaxies agree with observations from late-type Sbc/d galaxies. Also, SN Ia rates of simulations adopting 0.03 as the fraction of binary systems that host SNe Ia are in keeping with observations of Sbc/d galaxies.

(iii) We investigated stellar and gas metallicity gradients in simulations: negative radial abundance profiles are recovered, thus in agreement with observations. Slopes of profiles agree with observations, pointing to the effectiveness of our model to properly describe the chemical enrichment of the galaxy at different positions.

(iv) We compared gas metallicity profiles from our set of simulations with the oxygen abundance radial profiles of 130 nearby disc galaxies (Pilyugin et al. 2014). We found that a Kroupa et al. (1993) IMF leads to a lower amount of metals produced by massive stars and supplied to the ISM, resulting in a better agreement with observations. Therefore, we can argue that an IMF more top-light than Kroupa (2001) and Chabrier (2003) has to be preferred for local disc galaxies.

(v) We investigated the stellar $\alpha$-enhancement of star particles in our simulations, and considered also chemical patterns associated with disc and bulge, separately. The best agreement with observations of MW stars is retrieved when the Kroupa (2001) IMF is assumed.

(vi) We quantified the effect of chemical feedback from outflows, investigating the mass of metals that is distributed at an increasing distance from the galaxy centre. We verified that galactic outflows in our simulations are effective in driving metals out from the sites of star formation: if a high amount of metals in the ISM is present, this cannot be ascribed to the inability of outflows to move enriched

---

[7]We postpone the analysis of the time evolution of the cooling rate for models adopting different sets of stellar yields to a future study.
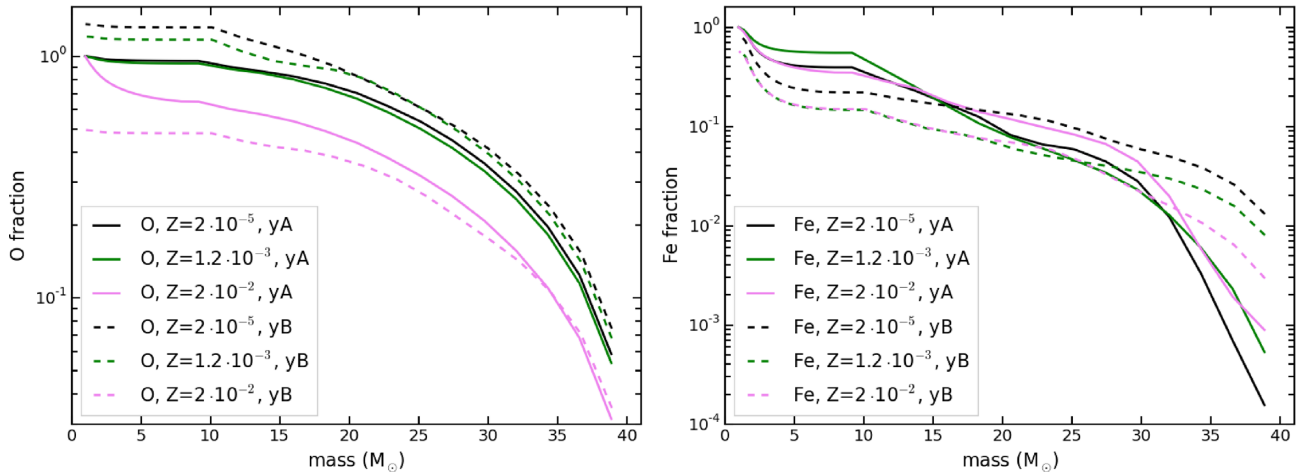
**Figure 17.** Cumulative mass in oxygen (left-hand panel) and iron (right-hand panel) that is (newly) produced by an SSP as a function of the mass of stars in the SSP. Solid and dashed curves refer to the sets A and B of stellar yields, respectively. Curve of each considered metallicity are normalized to the maximum of the curve of the set A. We consider the K3s IMF. We analyse three possible values for the metallicity Z: $2 \times 10^{-5}$ (black), $1.2 \times 10^{-3}$ (green), and $2 \times 10^{-2}$ (pink).

gas outwards. We found that the mass of metals in gas within a distance of 20 kpc from the galaxy centre is ∼20 per cent of the metals produced, while about as many metals are associated with stars within the same distance. The mass of metals in gas and stars within 150 kpc from the galaxy centre increases to the ∼60 per cent of the synthesized metals. Therefore, an amount of metals as large as ∼40 per cent has been driven beyond 150 kpc by galactic outflows, which have promoted the circulation of metals in the CGM at high redshift, during the galaxy formation process.

In the light of these results, we can draw the following conclusions on the different ingredients entering in the adopted model of stellar evolution.

(i) Assuming either a Kroupa et al. (1993) IMF or a Kroupa (2001) IMF results in different star formation histories, stellar feedback and scenarios of chemical evolution.

(ii) If observational metallicity estimates are not affected by significant uncertainties, the Kroupa (2001) IMF is more suitable for our Galaxy, while a Kroupa et al. (1993) IMF (more top-light) should be preferred for other disc galaxies in the local universe. We predict that MW stars exhibit a higher metal content with respect to other nearby late-type galaxies.

(iii) Our analysis supports a value for the fraction of binary systems suitable to give rise to SNe Ia of 0.03. This rules out the commonly adopted value 0.1, at least for late-type galaxies and when the IMFs that we are adopting are considered. Evidences that corroborate this finding come from the comparison of predicted SN rates and stellar $\alpha$-enhancement with observations.

(iv) Adopted stellar yields are a key component of the chemical model, as they control cooling and drive star formation. Different yields lead to different chemical features. The pattern of chemical enrichment for stars located in the galaxy bulge shows that the bulge component is the most sensitive to stellar yields.

As already pointed out, the availability of further accurate data from ongoing surveys could alleviate the tension between discrepant results and lead to firmer conclusions. As a concluding remark, we stress that an emerging piece of evidence of our work is that it is not trivial to simulate galaxies with a dominant disc component and

an almost quiescent low-redshift SFR that simultaneously match all the available observational constraints on the pattern of metal enrichment of both the gas and stellar components. Also, results are far from being predictable when a single ingredient entering in the model for chemical evolution is varied, as its effect has a complex interplay with processes regulating the star formation history and shaping the morphology of simulated galaxies. Our results highlight that it is challenging to reproduce at the same time observations of metal abundance in gas and stars. Observational uncertainties and issues with the calibration of metallicity estimates could definitely enter and complicate the comparison with simulation predictions. However, our analysis also highlights that the numerical modelling of the share of metals between stars and the surrounding gas is of paramount importance, and should be further investigated. To pursue that, higher resolution simulations are mandatory, as well as a proper treatement of the diffusion of metals associated with turbulent gas motions (see e.g. Pilkington et al. 2012; Williamson, Martel & Kawata 2016).

The detailed and accurate investigation of the chemical evolution of a single galaxy that we have presented in this work is the starting point of a systematic analysis that we plan to accomplish in future works. A natural and desirable extension of this study is indeed the simulation of cosmological boxes, where statistical properties of a population of galaxies can be examined.

As a word of caution, we note that the simulations presented in this work do not include the effect of the AGN feedback. Albeit the AGN feedback is not expected to play a major role in the overall evolution of late-type galaxies nor to influence the history of chemical enrichment of the galaxy significantly, it can however play a supporting role in fostering outflows and promoting the circulation of metals over galactic scales. We postpone the investigation of the effect of the AGN feedback to a forthcoming paper.

# REFERENCES

Asplund M., Grevesse N., Sauval A. J., Scott P., 2009, ARA&A, 47, 481
Aumer M., White S. D. M., Naab T., 2014, MNRAS, 441, 3679
Barber C., Crain R. A., Schaye J., 2018, MNRAS, 479, 5448
Barbuy B., Chiappini C., Gerhard O., 2018, ARA&A, 56, 223
Barden M. et al., 2005, ApJ, 635, 959
Beck A. M. et al., 2016, MNRAS, 455, 2110
Bekki K., 2013, MNRAS, 436, 2254
Biffi V. et al., 2017, MNRAS, 468, 531
Bono G., Marconi M., Cassisi S., Caputo F., Gieren W., Pietrzynski G., 2005, ApJ, 621, 966
Borgani S., Fabjan D., Tornatore L., Schindler S., Dolag K., Diaferio A., 2008, Space Sci. Rev., 134, 379
Bouché N., Lehnert M. D., Péroux C., 2005, MNRAS, 364, 319
Bovy J., Hogg D. W., Rix H.-W., 2009, ApJ, 704, 1704
Caffau E., Ludwig H.-G., Steffen M., Freytag B., Bonifacio P., 2011, Sol. Phys., 268, 255
Cappellari M. et al., 2012, Nature, 484, 485
Cayrel R. et al., 2004, A&A, 416, 1117
Chabrier G., 2003, PASP, 115, 763
Chiappini C., Matteucci F., Gratton R., 1997, ApJ, 477, 765
Chiappini C., Matteucci F., Romano D., 2001, ApJ, 554, 1044
Chiosi C., Bressan A., Portinari L., Tantalo R., 1998, A&A, 339, 355
Clemens M. S., Bressan A., Nikolic B., Rampazzo R., 2009, MNRAS, 392, L35
Conroy C., van Dokkum P. G., 2012, ApJ, 760, 71
de Laverny P., Recio-Blanco A., Worley C. C., De Pascale M., Hill V., Bijaoui A., 2013, The Messenger, 153, 18
De Lucia G., Tornatore L., Frenk C. S., Helmi A., Navarro J. F., White S. D. M., 2014, MNRAS, 445, 970
De Masi C., Matteucci F., Vincenzo F., 2018, MNRAS, 474, 5259
Doherty C. L., Gil-Pons P., Lau H. H. B., Lattanzio J. C., Siess L., 2014a, MNRAS, 437, 195
Doherty C. L., Gil-Pons P., Lau H. H. B., Lattanzio J. C., Siess L., Campbell S. W., 2014b, MNRAS, 441, 582
Dolag K., Mevius E., Remus R.-S., 2017, Galaxies, 5, 35
Dutton A. A. et al., 2011, MNRAS, 410, 1660
Edvardsson B., Andersen J., Gustafsson B., Lambert D. L., Nissen P. E., Tomkin J., 1993, A&A, 275, 101
Ferrara A., Scannapieco E., Bergeron J., 2005, ApJ, 634, L37
Few C. G., Courty S., Gibson B. K., Michel-Dansac L., Calura F., 2014, MNRAS, 444, 3845
Fontanot F., De Lucia G., Hirschmann M., Bruzual G., Charlot S., Zibetti S., 2017, MNRAS, 464, 3812
Gallazzi A., Brinchmann J., Charlot S., White S. D. M., 2008, MNRAS, 383, 1439
Gargiulo I. D. et al., 2015, MNRAS, 446, 3820
Genovali K. et al., 2013, A&A, 554, A132
Genovali K. et al., 2014a, VizieR Online Data Catalog, 356

Genovali K. et al., 2014b, A&A, 566, A37
Gibson B. K., Fenner Y., Renda A., Kawata D., Lee H.-c., 2003, PASA, 20, 401
Gillessen S., Eisenhauer F., Trippe S., Alexander T., Genzel R., Martins F., Ott T., 2009, ApJ, 692, 1075
González Delgado R. M. et al., 2014, A&A, 562, A47
Grand R. J. J. et al., 2016, MNRAS, 460, L94
Grand R. J. J. et al., 2018a, MNRAS, 481, 1726
Grand R. J. J. et al., 2018b, MNRAS, 474, 3629
Greggio L., Renzini A., 1983, A&A, 118, 217
Grisoni V. et al., 2017, MNRAS, 472, 3637
Gutcke T. A., Springel V., 2019, MNRAS, 482, 118
Haardt F., Madau P., 2001, in Neumann D. M., Tran J. T. V., eds, Clusters of Galaxies and the High Redshift Universe Observed in X-rays. CEA, Saclay, p. 64
Karakas A., Lattanzio J. C., 2007, PASA, 24, 103
Karakas A. I., 2010, MNRAS, 403, 1413
Kewley L. J., Ellison S. L., 2008, ApJ, 681, 1183
Kroupa P., 2001, MNRAS, 322, 231
Kroupa P., 2002, Science, 295, 82
Kroupa P., Weidner C., 2003, ApJ, 598, 1076
Kroupa P., Tout C. A., Gilmore G., 1993, MNRAS, 262, 545
Kroupa P., Weidner C., Pflamm-Altenburg J., Thies I., Dabringhausen J., Marks M., Maschberger T., 2013, The Stellar and Sub-Stellar Initial Mass Function of Simple and Composite Populations. Springer-Verlag, Berlin, p. 115
La Barbera F., Ferreras I., Vazdekis A., de la Rosa I. G., de Carvalho R. R., Trevisan M., Falcón-Barroso J., Ricciardelli E., 2013, MNRAS, 433, 3017
Lecureur A., Hill V., Zoccali M., Barbuy B., Gómez A., Minniti D., Ortolani S., Renzini A., 2007, A&A, 465, 799
Lemasle B., François P., Bono G., Mottini M., Primas F., Romaniello M., 2007, A&A, 467, 283
Luck R. E., Lambert D. L., 2011, AJ, 142, 136
Luck R. E., Kovtyukh V. V., Andrievsky S. M., 2006, AJ, 132, 902
Luck R. E., Andrievsky S. M., Kovtyukh V. V., Gieren W., Graczyk D., 2011, AJ, 142, 51
Mannucci F., Della Valle M., Panagia N., Cappellaro E., Cresci G., Maiolino R., Petrosian A., Turatto M., 2005, A&A, 433, 807
Maoz D., 2008, MNRAS, 384, 267
Matteucci F., 2003, The Chemical Evolution of the Galaxy. Kluwer Academic Publishers, Dordrecht
Matteucci F., Francois P., 1989, MNRAS, 239, 885
Matteucci F., Gibson B. K., 1995, A&A, 304, 11
Matteucci F., Greggio L., 1986, A&A, 154, 279
Meléndez J. et al., 2008, A&A, 484, L21
Mikolaitis Š., de Laverny P., Recio-Blanco A., Hill V., Worley C. C., de Pascale M., 2017, A&A, 600, A22
Mott A., Spitoni E., Matteucci F., 2013, MNRAS, 435, 2918
Muñoz-Mateos J. C., Boissier S., Gil de Paz A., Zamorano J., Kennicutt R. C. Jr, Moustakas J., Prantzos N., Gallego J., 2011, ApJ, 731, 10
Murante G., Monaco P., Giovalli M., Borgani S., Diaferio A., 2010, MNRAS, 405, 1491
Murante G., Monaco P., Borgani S., Tornatore L., Dolag K., Goz D., 2015, MNRAS, 447, 178
Nagashima M., Lacey C. G., Okamoto T., Baugh C. M., Frenk C. S., Cole S., 2005, MNRAS, 363, L31
Nomoto K., Kobayashi C., Tominaga N., 2013, ARA&A, 51, 457
Oppenheimer B. D., Davé R., Katz N., Kollmeier J. A., Weinberg D. H., 2012, MNRAS, 420, 829
Oppenheimer B. D., Schaye J., Crain R. A., Werk J. K., Richings A. J., 2018, MNRAS, 481, 835
Padovani P., Matteucci F., 1993, ApJ, 416, 26
Patel S. G. et al., 2013, ApJ, 778, 115
Pedicelli S. et al., 2010, A&A, 518, A11
Peeples M. S., Werk J. K., Tumlinson J., Oppenheimer B. D., Prochaska J. X., Katz N., Weinberg D. H., 2014, ApJ, 786, 54

Pettini M., 2006, in Le Brun V., Mazure A., Arnouts S., Burgarella D., eds, Proc. of the Vth, The Fabulous Destiny of Galaxies: Bridging Past and Present. Frontier Group, Paris, p. 319

Pichon C., Pogosyan D., Kimm T., Slyz A., Devriendt J., Dubois Y., 2011, MNRAS, 418, 2493

Pilkington K. et al., 2012, MNRAS, 425, 969

Pillepich A. et al., 2018, MNRAS, 473, 4077

Pilyugin L. S., Grebel E. K., Kniazev A. Y., 2014, AJ, 147, 131

Romaniello M. et al., 2008, A&A, 488, 731

Romano D., Karakas A. I., Tosi M., Matteucci F., 2010, A&A, 522, A32

Romano D., Matteucci F., Zhang Z.-Y., Papadopoulos P. P., Ivison R. J., 2017, MNRAS, 470, 401

Sagar R., Richtler T., 1991, A&A, 250, 324

Salpeter E. E., 1955, ApJ, 121, 161

Scannapieco C. et al., 2012, MNRAS, 423, 1726

Scannapieco C., White S. D. M., Springel V., Tissera P. B., 2009, MNRAS, 396, 696

Scannapieco C., Gadotti D. A., Jonsson P., White S. D. M., 2010, MNRAS, 407, L41

Schaye J. et al., 2015, MNRAS, 446, 521

Snaith O. N., Haywood M., Di Matteo P., Lehnert M. D., Combes F., Katz D., Gómez A., 2014, ApJ, 781, L31

Spina L. et al., 2017, A&A, 601, A70

Spitoni E., Matteucci F., 2011, A&A, 531, A72

Springel V. et al., 2008, MNRAS, 391, 1685

Springel V., 2005, MNRAS, 364, 1105

Springel V., Hernquist L., 2003, MNRAS, 339, 289

Sziládi K., Vinkó J., Poretti E., Szabados L., Kun M., 2007, A&A, 473, 579

Thielemann F.-K. et al., 2003, in Hillebrandt W., Leibundgut B., eds, From Twilight to Highlight: The Physics of Supernovae. Springer-Verlag, Berlin, p. 331

Tinsley B. M., 1979, ApJ, 229, 1046

Tornatore L., Borgani S., Dolag K., Matteucci F., 2007, MNRAS, 382, 1050

Torrey P. et al., 2017, MNRAS, preprint (arXiv:1711.05261)

Tumlinson J., Peeples M. S., Werk J. K., 2017, ARA&A, 55, 389

Valentini M., Murante G., Borgani S., Monaco P., Bressan A., Beck A. M., 2017, MNRAS, 470, 3167

Valentini M., Bressan A., Borgani S., Murante G., Girardi L., Tornatore L., 2018, MNRAS, 480, 722

van Dokkum P. G. et al., 2013, ApJ, 771, L35

Veilleux S., Cecil G., Bland-Hawthorn J., 2005, ARA&A, 43, 769

Venn K. A., Irwin M., Shetrone M. D., Tout C. A., Hill V., Tolstoy E., 2004, AJ, 128, 1177

Vogelsberger M. et al., 2018, MNRAS, 474, 2073

Vogelsberger M., Genel S., Sijacki D., Torrey P., Springel V., Hernquist L., 2013, MNRAS, 436, 3031

Wiersma R. P. C., Schaye J., Smith B. D., 2009a, MNRAS, 393, 99

Wiersma R. P. C., Schaye J., Theuns T., Dalla Vecchia C., Tornatore L., 2009b, MNRAS, 399, 574

Williamson D., Martel H., Kawata D., 2016, ApJ, 822, 91

Woosley S. E., Weaver T. A., 1995, ApJS, 101, 181

Yates R. M., Henriques B., Thomas P. A., Kauffmann G., Johansson J., White S. D. M., 2013, MNRAS, 435, 3500

Yong D., Carney B. W., Teixera de Almeida M. L., Pohl B. L., 2006, AJ, 131, 2256

Zoccali M. et al., 2006, A&A, 457, L1

This paper has been typeset from a TEX/LATEX file prepared by the author.